Effect of M^{2+} Ions on the Magnetic, Dielectric and Optical Properties of MFe_2O_4 (M-Co, Ba) Ferrites

Dissertation submitted to the

Kerala University in partial fulfillment of requirements

for the degree of

MASTER OF SCIENCE

In

PHYSICS

University of Kerala

Project report 2020-2022

Abstract

In this work, we synthesized pristine $CoFe_2O_4$ and BaF_2O_4 and investigate their structural, optical, dielectric and magnetic properties. Both $CoFe_2O_4$ and $BaFe_2O_4$ were prepared via the citric acid-assisted sol-gel auto combustion method. X-ray diffraction studies were performed to elucidate the structure of these samples. A computer program called Qualx software is used to identify the crystal phases and the presence of impurities. From the database, It is seen that $CoFe_2O_4$ exhibits a mixed spinel cubic structure with a space group *Fd-3m* and $BaFe_2O_4$ exhibits an orthorhombic structure with a space group $Cmc2_1$. Rietveld refinement analysis is performed to obtain a complete picture of crystal structure and cation distribution. It is observed that $CoFe_2O_4$ exhibit a centrosymmetric structure having two origins from octahedral and tetrahedral sites and $BaFe_2O_4$ have a centrosymmetric structure. The position and occupancy of the atoms in both compounds are identified. Williamson Hall method is employed to study the crystallite size and induced strain in $CoFe_2O_4$ and $BaFe_2O_4$ material. Optical properties were identified by UV-Visible spectroscopy. The low density of defect states is observed in $BaFe_2O_4$. $BaFe_2O_4$ exhibit low dielectric permiitivity and low tangent loss in room temperature. Isothermal M-H loop at room temperature shows that $CoFe_2O_4$ exhibit a ferrimagnetism and $BaFe_2O_4$ exhibit a ferrimagnetism with antiferromagnetism.

Contents

List of Figures

List of Tables

Chapter 1
General Introduction

1.1 Dielectric Materials

Based on conductivity, materials can be divided into three, (i) Conductor, (ii) Semiconductor and (iii) Insulator. The dielectric material is an insulator that can be polarized by an applied electric field. When a dielectric material is placed in an electric field, electric charges do not flow through the material, as they have no loosely bound or free electrons that may drift through the material, instead the positive and negative charges slightly shifted from their equilibrium position and cause polarization. Positive charges are displaced in the direction of the field and negative charges shift in the opposite direction. This creates an internal electric field that reduces the overall field within the dielectric itself.

1.1.1 Dipole Moment

An electric dipole is an entity in which equal and opposite charges are separated by a small distance. The moment of a dipole of two equal and opposite charges +q and –q separated by a distance r is defined as, p = qr and is directed from the negative to positive charge. The total dipole moment is defined as $p = \Sigma q_n r_n$, where r_n is the position vector of the charge q_n [1].

1.1.2 Polarization

The polarization P is defined as the dipole moment per unit volume, i.e., $P = \frac{p}{\Delta V}$. If the number of molecules per unit volume is N and if each has a moment p, then the polarization is given by P = Np. The mechanism of polarization is different for non-polar and polar dielectric materials [1].

1.1.3 Dielectric Constant

The dielectric constant (also known as the permittivity of the medium) is a measure of the degree to which a medium can resist the flow of charge. It is defined as the ratio for the electric displacement D to the electric field intensity E, i.e.

$$\epsilon = \frac{D}{E} = \epsilon_r \epsilon_0 \qquad (1)$$

Where ϵ_r is the relative permittivity of the medium and ϵ_0 is the permittivity of free space. The relative dielectric constant $\epsilon_r = \epsilon / \epsilon_0$ expresses the properties of the medium All the dielectric and optical properties of the substance are contained in this constant [1].

1.1.4 Polarizability

When an electric field is applied to a solid, electric charge are displaced causing polarization in it. The induced dipoles of moments p are proportional to the local field E_{loc} i.e.,

$$p = \alpha E_{loc} \qquad (2)$$

where **α** is known as the electrical polarizability of the atom. The electric field acting at an atom in a dielectric is known as the polarizing field or the local field E_{loc} [1].

1.1.5 Different types of polarization processes

Total polarization induced in dielectrics is the sum of four sources of charge displacement expressed as,

$$P_t = P_i + P_o + P_e + P_s \qquad (3)$$

1.1.5.1 Electronic polarization

Electronic polarization (P_e) occurs when an electric field distorts the negative cloud of electrons around positive atomic nuclei in a direction opposite the field. This shifting of electrons and nuclei from the equilibrium position gives an induced dipole moment. The electronic polarizability $\alpha_e = e^2 / m (\omega_0^2 - \omega^2)$, where ω is the frequency of the local field. This contribution is common in all solids [2].

1.1.5.2 Ionic polarization

In ionic polarization (P_i**)** the negative ions of the molecules will tend to shift towards the positive side of the applied field and positive ions will tend to shift towards the negative side of the applied electric field. This shifting of ions produces polarization. Ionic polarizability $\alpha_i = e^2/\beta$ where β is the force constant. This contribution is significant in alkali halides and other ionic solids [1,2].

1.1.5.3 Orientational polarization

Orientational polarization (P_o) also known as dipolar polarization is found in polar dielectrics that possess permanent dipole moments. In the absence of an electric field, the permanent molecular dipoles are distributed randomly in all directions so that their net dipole moment is zero. In the presence of an external electric field, dipoles align along the direction of the field and the dielectric becomes polarized. Oriental polarizability per dipole $\alpha_i = p^2 / 3KT$ [2].

1.1.5.4 Space charge polarization

Space charge polarization also known as interfacial polarization occurs when there is an accumulation of charge at an interface between two materials or between two regions within a material because of an external field. This can occur when there is a compound dielectric, or when there are two electrodes connected to a dielectric material. Instead of affecting bound positive or negative charges, space charge polarization affects free charges as well. This polarization is usually observed in amorphous or poly-crystalline solids [3].

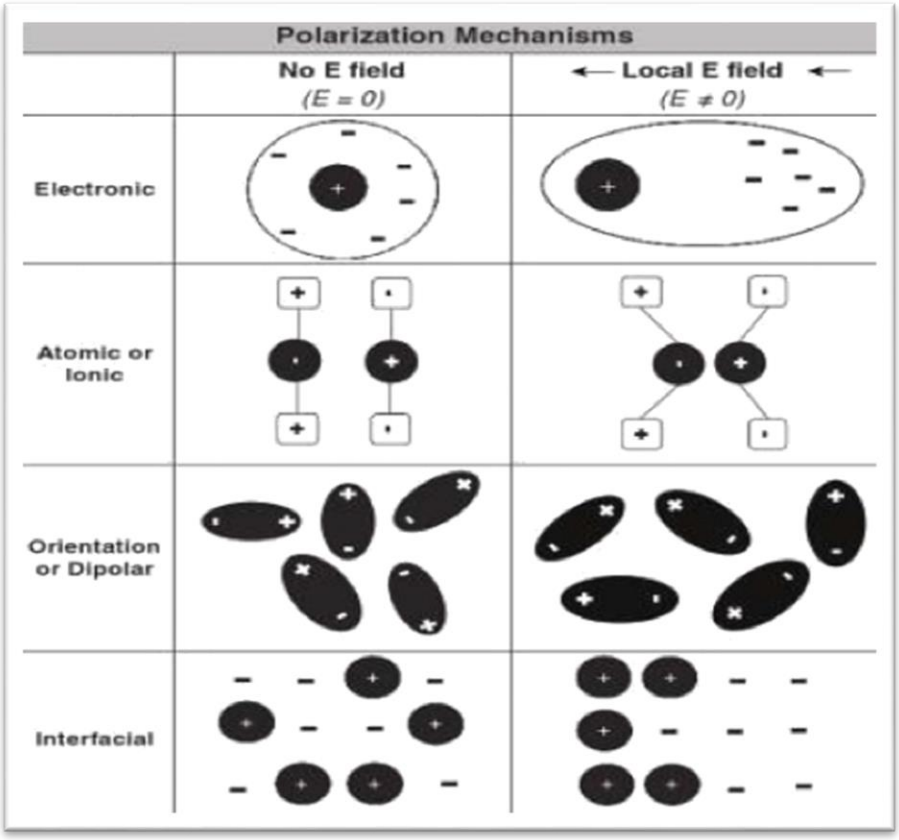

Figure 1.1 Polarization mechanisms in dielectrics [4]

1.1.6 Frequency effects on polarization

Total polarizability of dielectric decreases with an increase in the frequency of the applied electric field. Each type of polarization shows different frequency responses. As electronic displacement is very rapid electronic polarization occurs at frequencies up to10^{17} Hz. In the optical frequency range, dielectric constant arises almost entirely from the electronic polarizability. Ionic polarization is a bit slower and occurs at frequencies up to 10^{13}. Dipolar polarization occurs at frequencies less than 10^{10}. The ionic and dipolar contributions are small at higher frequencies due to the inertia of the ions and molecules. Space charge polarization is the slowest and occurs at less than 10^{4}.

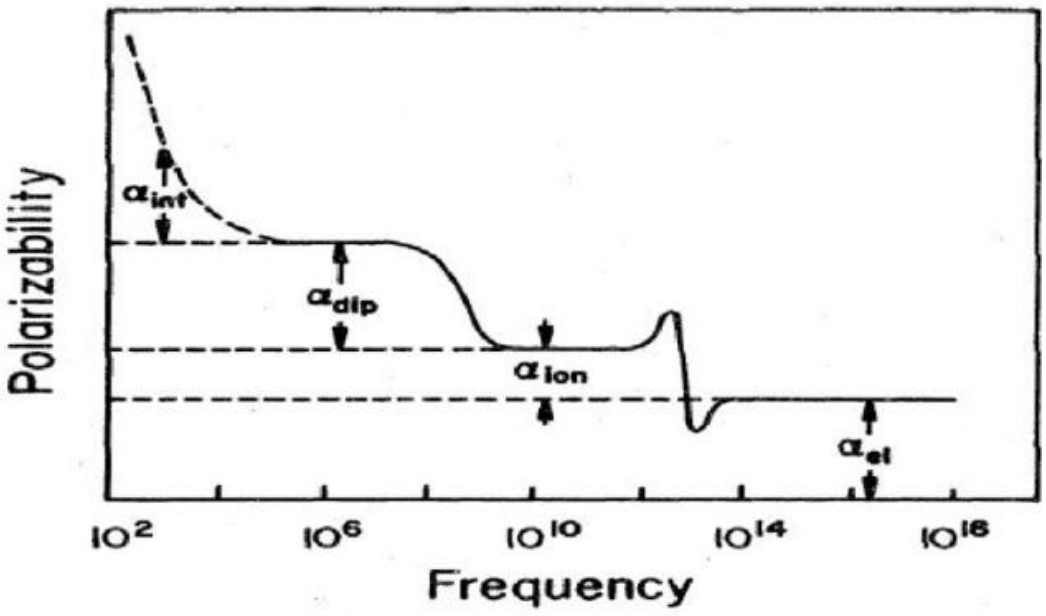

Figure 1.2 Frequency dependence of various polarization processes[5]

Dielectric polarization can be expressed as a function of temperature and is given by,

$$P(t) = P[1\text{-}\exp\text{-}(t/t_r)] \qquad (4)$$

where P is the maximum polarization and t_r is the relaxation time taken for the polarization process [6,7].

1.2 Magnetic materials

Magnetic materials are materials having a magnetic domain and are attracted or repelled by an external magnetic field. They play an important role in the industrial and scientific research field. Magnetism is mainly due the interaction of uncompensated magnetic

moments of constituent atoms or molecules. This section describes various quantities and parameters in magnetism

1.2.1 Various quantities and parameters in magnetism

Magnetic dipole moment

Magnetic dipole moment is the fundamental quantity of magnetism, denoted by m. The atomic theory of magnetism expresses magnetic dipole moment μ_m as,

$$\mu_m = -\left(\frac{e}{2m}\right) L \qquad (5)$$

The negative sign indicates magnetic moment is antiparallel to angular momentum. Magnetic moment can arise from three sources (i) orbital motion of electron, (ii) electron spin and (iii) spin of the nucleus [8].

Orbital magnetic moment: It is the measure of the strength of the magnetic field produced by the orbital angular momentum of an electron. Its magnitude is given by Bohr magneton (μ_B). It can be expressed as,

$$\mu_B = \frac{eh}{4\pi m} = 9.27\times 10^{-24}\ Am^2 \qquad (6)$$

Bohr magneton is a quantum of orbital magnetic moment. If an atom contains more than one electron, total orbital magnetic moment of an atom is an algebraic sum of orbital magnetic moment of individual electrons. Atoms with partially filled orbital have non zero magnetic moment [8].

Spin magnetic moment of electron: Magnetic moment due to the spin of the electron is taken by its components in z direction and it can be expressed as,

$$\mu_{sz} = \left(\frac{eh}{4\pi m}\right) m_s \qquad (7)$$

g is known as lande's splitting factor and m_s is known as magnetic spin quantum number it can only take either +1/2 or -1/2.

The spin magnetic moment of the nucleus: Magnetic moment is inversely proportional to particle mass. The mass of the nucleus is three order times greater than the electron therefore the magnetic moment of the nucleus will be three times lesser than the magnetic moment of the electron. Most of the time magnetic moments due to

the nucleus can be neglected. The magnetic moment due to the nucleus can be given by,

$$\mu_m = \frac{eh}{4\pi Mp} \qquad (8)$$

where Mp is the proton mass [8].

Magnetization(M): The state of material being magnetized or the process in which magnetic materials are magnetized or it can be said that magnetic dipole moment per unit volume of material.

Magnetic field intensity or magnetizing force (H): The externally applied magnetic field, the force experienced by the unit north pole.

Magnetic flux density (B): number of magnetic lines per unit area of the cross section.

Magnetic response in the medium due to the applied magnetic field can be measured by two parameters **permeability and susceptibility.**

Magnetic permeability (μ): The ratio of magnetic flux density (B) to magnetic field intensity (H). It is the property of the material which allows magnetic lines of force to penetrate the material. $\mu = B/H$

Relative permeability (μ_r): the ratio of permeability of free space to the permeability of the material.

Magnetic susceptibility(χ): the ratio of magnetization (M) to magnetic field intensity(H) and is indicative of the ease with which a material can be magnetized by an applied magnetic field. χ can be both positive and negative. $\chi = M/H$

The relation between susceptibility and permeability is given by $\mu = 1+ \chi$ [8]

1.2.2 Classification of magnetic materials

Depending on the structure, the electronic configuration of the atoms and the response to external magnetic field materials are classified into five classes.

Diamagnetism

A diamagnetic material is one in which all the atoms have paired electrons in the shells. Thus the net magnetic moment of the atom is zero. However, when an external

magnetic field is applied these materials get magnetized opposite to the applied field direction. Thus they have negative magnetization and negative susceptibility. Diamagnetic susceptibility is independent of temperature. E.g.: aluminium oxide, silver, gold, silicon, copper etc [8].

Paramagnetism

In these materials, the atoms or ions have unpaired electrons in partially filled orbitals. Each atom has a small net magnetic moment. But there is no interaction between these atomic magnets. In the absence of an external field, dipoles exist with random orientation; in the presence of a field, dipoles are aligned along the field direction. Susceptibility has a small positive value and is inversely proportional to the absolute temperature. Eg: alkali metals, transition metals, and rare earth metals [8].

Ferromagnetism

In these materials permanent dipoles are present. A spinning electron behaves as a tiny magnet. There exists a strong interaction between the atomic magnets. These interaction forces are exchange types of forces. The interaction force between the atoms is due to the exchange of electrons. Atomic magnets are aligned parallel to each other under the influence of these exchange forces even in the absence of an external magnetic field. Thus they have spontaneous magnetization. According to Weiss ferromagnets are divided into small regions in their demagnetized state and these regions are known as domains. These domains are spontaneously magnetized in various directions and the net magnetization of the material is the vector sum of each domain magnetization. On the application of the field these domains orient in the direction of the field and increases the magnetization of the material. Ferromagnet shows paramagnetism above Curie temperature T_C. Eg: iron-nickel, and cobalt [8].

Antiferromagnetism

Spin dipoles are equal and oriented in opposite directions. The net magnetic moment is zero in the absence of an external magnetic field. They show either insulating or semiconducting behaviour. Antiferromagnetic materials above a certain temperature become paramagnetic and this temperature is known as Neel temperature. Eg: salts of transition metals [8].

Ferrimagnetism

Spin dipoles are unequal and oriented in opposite directions. There is a net magnetic moment even in the absence of an external magnetic field thus showing spontaneous magnetization at room temperature like ferromagnetic materials. Eg: ferrites [8]

1.3 Ferrites

Ceramic-like ferrimagnetic materials, which are mainly composed of ferric oxide, Fe_2O_3, are called ferrites. The history of ferrites began with the discovery of the black ore magnetite (Fe_3O_4), which is a natural mineral, is a genuine ferrite, which would attract iron. Magnetite has been discovered many centuries ago and found its first application in the mariner's compass. However, the first attempt to prepare various types of ferrites was made at the beginning of the last century. The chemical formula of natural ferrite magnetite (Fe_3O_4) is $Fe^{2+}\ Fe_2^{3+}\ O_4$. The corresponding general formula is $M^{2+}\ Fe_2^{3+}\ O_4$, where M is a divalent metal such as Mn, Co, Ba, Ni, Cu, Mg, Zn, or Cd. Structural, electrical, dielectric and magnetic properties of ferrites has a strong dependence on the preparation method. High-temperature solid state reaction, sol-gel technique, co-precipitation, pulsed laser deposition, and high-energy ball milling are some of the important methods for the preparation of ferrites in powder or thin film form [8,9].

Ferrites attracted researchers owing to their unique electrical and magnetic properties. Magnetic properties are the most important properties of ferrites which arise due to the spin moment of unpaired 3d electron of the transition element. Ferrites are a promising candidate for high-frequency devices. High saturation magnetization and high electrical resistivity make them suitable as cores for inductors and transformers. They have considerably low electrical loss with high chemical stability. Lower prices, greater heat resistance, higher corrosion resistance and easy manufacturing made them very popular. Ferrites find their applications from simple lifting magnets to the most complex microwave communication system employed in outer space. It is also used in satellite communication, radar, the memory of computers, radio, television, videotape etc. The most efficient power supplies used in electronic appliances are the switch mode power supplies which have ferrite as a major part. The possibility of preparing ferrites in the form of nanoparticles has opened a new and exciting research field, with

revolutionary applications not only in electronic technology but also in the field of biotechnology [10,11].

1.4 Classification of ferrites

Ferrites are classified based on two main criteria, crystal structure and magnetic properties. According to the crystal structure, there are four types of ferrites: spinel, hexagonal, garnet, and orthoferrites, while according to magnetic properties they are soft and hard ferrites [10,11].

1.4.1 Types based on the crystal structure

(a) **Spinel ferrites**

Spinel ferrites are characterized by a formula MFe_2O_4, where M stands for divalent metal ions. They crystallize in a cubic structure. The spinel lattice is composed of face-centred cubic close-packed oxygen anions. Two types of interstitial positions in the lattice are filled by metal ions or cations. A single unit cell consists of 96 interstitial positions of which 64 are tetrahedral sites, eight of which are occupied and 32 octahedral sites, sixteen of which are occupied. The Tetrahedral or A- the site is surrounded by four oxygen ions, and the octahedral or B- the site is surrounded by six oxygen ions. Spinel ferrites have high electrical resistivity and low magnetic losses.

In a normal spinel structure, divalent metal ions occupy the tetrahedral A sites while $2Fe^{3+}$ ions are at the octahedral B site. In inverse spinel ferrite, the A-site contains one trivalent ferric ion while the B site contains the remaining trivalent ferric ions and divalent metallic ions. The structure in which divalent metal ions and trivalent ferric ions are distributed at both A and B sites is termed random spinel ferrites [10].

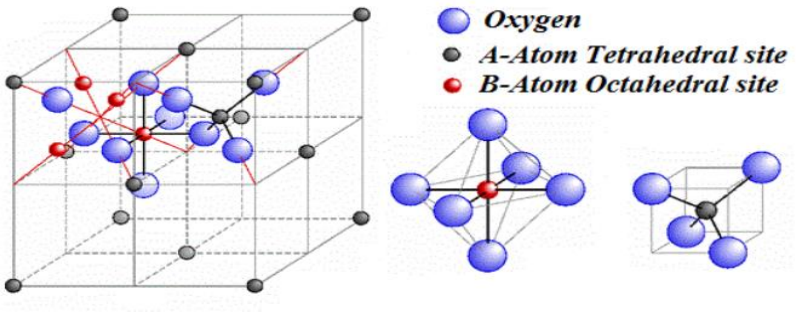

Figure 1.3 spinel ferrite unit cell structure [12]

(b) **Garnet**

Garnet ferrites are represented by a general formula $X_3Fe_5O_{12}$, containing two metal ions, one is iron and another is rare earth like Sm, Eu, Gd, Er, Tm, Lu, or Y. Trivalent cations (rare earth and Fe^{3+})occupy tetrahedral, octahedral, or dodecahedral (12-coordinated) sites and oxygen polyhedral surrounds the cations. Their unit shell shape is cubic. Garnet ferrites are used in microwave, acoustic, optical, and magneto-optical applications [10].

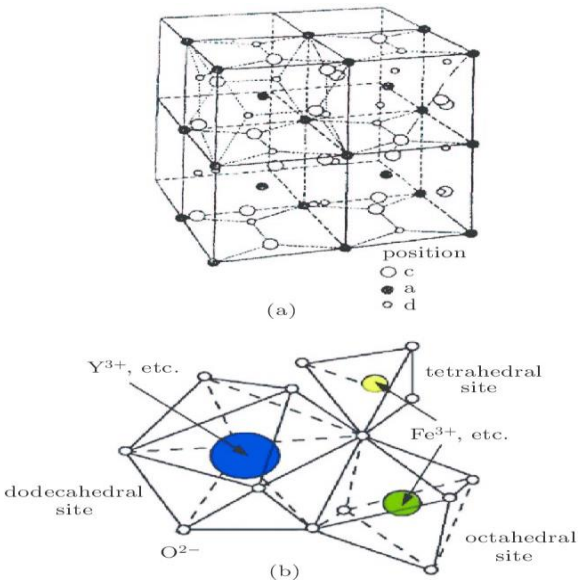

(a) Lattice structure (b) interstitial site

Figure 1.4 Garnet structure [13]

(c) Hexagonal ferrites

Hexagonal ferrites are presented by $MFe_{12}O_{19}$, where M is an element like Ba, Sr, Ca, or Pb, etc. They are also called rhombohedral ferromagnetic oxides. It has a close-packed hexagonal crystal structure. It has a major preferred axis called the c-axis. The complex crystal structure of hexaferrite has a superposition of S, R and T blocks along the c-axis. S block is a spinel block consisting of two oxygen layers (O_4-O_4) with Fe_6O_8 composition. R is a three-oxygen layer block (O_4-BaO_3-O_4) with $BaFe_6O_{11}$ composition. T block has four layers of oxygen ions (O_4-BaO_3-BaO_3-O_4) with $Ba_2Fe_8O_{14}$ composition. Hexaferrites are used in injection-moulded pieces, microwave devices, magnetic recording media, and radar-absorbing paints for military aircraft. Hexaferrites have a high coercivity and thereby, have widely been used as a permanent magnet as their direction of magnetization cannot be changed easily to another axis.

Barium ferrite ($BaFe_{12}O_{19}$) and strontium ferrite ($SrFe_{12}O_{19}$) are examples of hexaferrite [10,11].

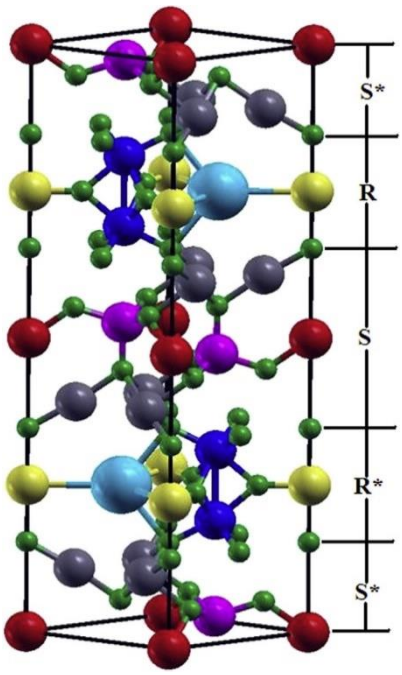

Figure 1.5 Crystal structure of M-type barium hexaferrite $BaFe_{12}O_{19}$ [14]

(d) Ortho ferrites

Ortho ferrite is structurally represented by $MFeO_3$, where M is a rare earth ion. In the perovskite structure A-site, i.e, corners of the cube, occupies large divalent or trivalent ions and the B-site, i.e, the centre of the cube occupies small trivalent or tetravalent metal ions. The oxygen ions are situated centrally on the facets of the cube. Orthoferrites are used in communication techniques, in sensors of magnetic fields and in optical internet [10,11].

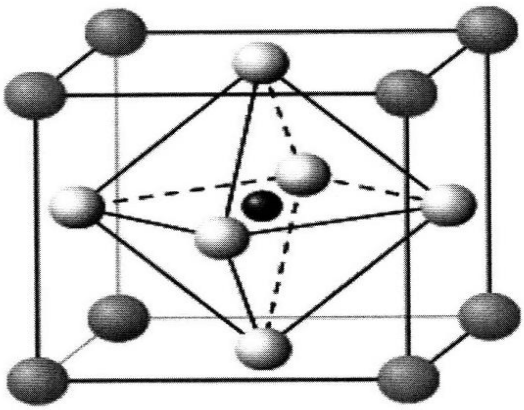

Figure 1.6 Perovskite structure of an orthoferrite [15]

1.4.2 Types based on magnetic properties

(a) Soft ferrites

Soft ferrites are ceramic electromagnetic materials. They have a homogenous cubic spinel crystalline structure and are represented by $MO.Fe_2O_3$, where M is a transition metal ion like iron, nickel, manganese, or zinc. They are ferromagnetic materials showing temporary magnetism, i.e, ferromagnetism emerges only when a magnetic field is applied. It is easily magnetized and demagnetized so that it can store or transfer magnetic energy in alternating or other changing waveforms. The most important soft ferrites are Mn-Zn ferrites and Ni-Zn ferrites. Soft ferrites are used for transformer cores, switch mode power supplies, inductors, convertors, electromagnetic interference filters, picture tubes, yokes and other applications where electromagnetic materials are required to operate at high frequencies.

(b) Hard ferrites

For hard ferrites, strong magnetization remains even after removing the applied magnetizing Field. Hard ferrites possess magnetism which is essentially permanent. They are composed of iron and barium or strontium oxides. Hard ferrites are used in the microwave, recording media, magneto-optic media, telecommunication, and electronic devices.

1.5 Applications of spinel ferrites

High-frequency components

In high-frequency applications, the common technique of reducing eddy current losses using iron cores becomes less efficient. Moreover, the existing switched mode power supply industries required even low energy losses in power conservation with the maintenance of adequate initial permeability. Manganese-zinc ferrite with low magnetic loss, high saturation magnetization, high permeability, and high magnetic domain relaxation frequency was achieved. This type of ferrite material is applied in electronic and electrical industries for manufacturing deflection yoke rings, memory chips, magnetic recording heads, transformers, transducers and other devices [16].

Microwave absorption

Radio broadcasting, satellite communications, radars, GPS, cellphones, and wireless networks operate in the microwave frequency range. The efficiency of these systems can be affected by unwanted reflections or emissions in addition to associated health risks. Ferrites can be used here for reflection suppression or damping of free space electromagnetic waves. $MnFe_2O_4$/wax, RGO/$MnFe_2O_4$/wax and the RGO/ $MnFe_2O_4$/PVDF are some of the excellent wave-absorbing ferrites in the microwave frequency range [16].

Supercapacitors

$CoFe_2O_4$, $SnFe_2O_4$, and many other metal ferrites are used for charge storage applications. The ferrites in various morphologies influence varying the surface area of the material leading to different super capacitance values. Charge storage capacity increases with surface area. The ferrites are observed to have a specific capacitance value of around 50-400 F/g. The fascinating electrochemical activities of several ferrite nanocomposites make them a potential candidate for supercapacitor applications [16].

Sensors and biosensors

Ferrite nanoparticles are widely used as sensor materials for detecting different analytes at trace levels. $CoFe_2O_4$ plays an important role in the fabrication of gas sensors. CO_2 gas sensors use Cobalt- manganese ferrites. Sensing accuracy, low detection levels of the analyte, and quick analysis time of ferrites make them suitable for electrochemical biosensors [16].

Photocatalytic activity

Ferrites have a characteristic behaviour of absorbing light with a bandgap of 1.1-2.3 eV. They are one of the most promising photocatalysts and can be separated and reused as they are magnetically separable. The spinel structure of ferrites provides extra catalytic reaction sites resulting in enhanced photocatalytic degradation efficiency [16].

1.6 Cobalt Ferrite

Recently metal-oxide nanoparticles have been the subject of study of much interest because of their unusual optical, electrical and magnetic properties. Ferrites are a broad class of magnetic oxides with high electrical resistivity, mechanical hardness, relatively

low cost and excellent dielectric and magnetic properties [17,18]. There are different types of ferrite, in which spinel ferrites gained much significance due to their exceptional electrical and magnetic properties. Cobalt ferrite $CoFe_2O_4$ is a well-known hard magnetic material [19]. CFO has an inverse spinel structure in which Co^{2+} ions occupy octahedral B sites and Fe^{3+} ions distribute equally between tetrahedral A sites and octahedral B sites [20]. Cobalt ferrite has gained wide attention due to its high coercivity, strong crystalline anisotropy, moderate magnetisation and high Curie temperature [21]. These properties along with their great chemical and physical stability [17] make CFO suitable for lithium-ion battery [21,22], high-density data storage [21], magnetic recording[20], magnetic fluids [21], magnetic drug delivery, catalysis, biosensors and hyperthermia [23,24]. Thus CFO has many potential values for magnetic and electric applications. The dielectric properties of CFO depend on the sintering temperature and time, heating rate, cooling rate etc [25,26]. unique magnetic properties depend on shape, size and purity which are sensitive to the synthesis method [21]. The different synthesis methods employed are co-precipitation, hydrometallurgical processes, sol-gel process, complexometric method microwave and so on.

1.7 Barium Ferrite

$BaFe_2O_4$ consists of twin components and the symmetry of the component crystal is orthorhombic. The unit cell contains eight formula units. Each iron atom is surrounded tetrahedrally by four oxygen atoms, with Fe-O distance ranging from 1.80 to 1.93 while there are two kinds of barium atoms, one surrounded by seven oxygen atoms with the Ba-O distance ranging from 2.62 to 2.94 A^0 and the other by eleven oxygen atoms at distances ranging from 2.74 to 3.34. The arrangement of the atoms is not a close-packed one. The intrinsic properties of $BaFe_2O_4$ nanoparticles such as high magnetic saturation and coercivity, high chemical and mechanical resistance and high Curie temperature have indicated that it is a good candidate for microwave devices, radar-absorbent materials, permanent magnets, photocatalysis, drug deliveries, credit cards etc. In recent years barium ferrite is highly used in the development of pigments for the production of tiles, ceramic coatings and cosmetics. Diverse methods have been used to prepare $BaFe_2O_4$ nanoparticles such as spray pyrolysis, co-precipitation, microemulsion, ball milling, and hydrothermal approaches. Extensive research is

performed to improve the synthesis methods to increase crystal purity, decrease the size, and control the morphology of the nanostructures [27–30].

1.8 Literature review

k. Maaz *et.al.*, synthesized magnetic nanoparticles of $CoFe_2O_4$ by wet chemical method along with heat treatment at 600^0c.XRD and TEM confirmed the formation of single-phase $CoFe_2O_4$ nanoparticles with inverse spinel structure in the range of 15-48 nm. The size of the particle increases with annealing temperature and time due to the enhancement in the coalescence process. They observed very large coercivity(10.5K Oe) and low saturation magnetization (40.8 emu/g) at 77K in comparison with room temperature because of the growth of magnetic anisotropy at low temperature. Saturation magnetization has smaller values for small particles but larger particles have values approaching those of bulk. [31].

Zhenfa Zi *et. al.*, prepared cobalt ferrite nanoparticles by a modified chemical coprecipitation route. XRD results indexed to a single phase spinel structure with the space group Fd3m – $O^7_{h.}$ The lattice parameter was estimated as 8.385 A^0. FESEM showed that the grains appeared spherical with diameters ranging from 20 to 30 nm. There is a shift in curie temperature T_c, T_c in the process of increasing temperature was slightly higher than that in the process of decreasing temperature. It is explained as due to changed Co^{2+} ion redistribution in tetrahedral and octahedral sites on heating. The coercivity of the synthesized sample was lower than the theoretical value, which could be explained by the mono-domain structure and a transformation from a ferrimagnetic to a superparamagnetic state [32].

$CoFe_2O_4$ nanoparticles with a diameter of about 5nm were prepared by batch supercritical hydrothermal synthesis method. D. Zhao *et. al.* found that the characteristics of products depend on pH, temperature, mole ratio (r) of Co^{2+} to Fe^{2+} and the coexisting cations Na^+ and K^+. The maximum coercivity and saturation magnetization of $CoFe_2O_4$ prepared by this method were 340.6 Oe and 68.9 emu/g, respectively. The coercivity is low and saturation magnetization is high compared to samples prepared by other methods [33].

The influence of sintering temperature on the structural, magnetic and dielectric properties of $CoFe_2O_4$ prepared by the sol-gel auto-combustion method is studied by

Ru Zhang *et.al.,* All samples are spinel ferrite with cubic symmetry. An increase in sintering temperature from 900^0C to 1300^0C results in an increase in average grain size from 0.26μm to 0.83μm. the dielectric constant and loss tangent measurement showed strong dependence on the temperature at all frequencies. The saturation magnetization increased while the coercivity and remanent magnetization decreased with the increasing sintering temperature. The saturation magnetization value is ~87.32 emu/g at room temperature. The highest value of coercivity of all the samples was 1368.33 Oe for the samples sintered at 900^0C [34].

C.H. Yan *et. al.* have given a novel combustion method which is a rapid and reproducible route for the preparation of cobalt spinel ferrite using glycine as fuel. The materials produced are porous powders with a considerably large surface area. The magnetization and coercivity show a strong dependence on the G/N(glycine to nitrate) ratio in the range from 0.2 to 0.1. The novel combustion processing provides a convenient and fast approach to doping with foreign ions to modify the properties of Co ferrite [35].

Size-induced effect on nano-crystalline $CoFe_2O_4$ is studied by Vinod Kumar *et. al.,* with annealing there is no change in the crystalline phase of the particles. Grain growth was found to occur with an increase in annealing temperature and leads to a decrease in the specific surface area of the particles. Also, the strain factor has been much reduced for the particles annealed at higher temperatures. VSM show that the single-domain nano-magnetic particles possess higher coercivity as compared to samples below or above the single-domain size limit. Superparamagnetic size particles are best suitable for ferrofluid preparation [36].

Mukesh C. Dimri *et. al.,* synthesized Barium Monoferrite by citrate combustion method and heat treated in the temperature range 1100-1300℃. Orthorhombic crystal structure formation was confirmed from the XRD pattern. These samples have higher Curie temperatures and larger coercivity. This might be related to the synthesis by solution method, which resulted in fine grains and good exchange interactions. However, they exhibited lower saturation magnetization as compared to spinel barium Monoferrite and M-type barium hexaferrite. The change in Curie temperature after sintering at different temperatures could be due to modification in resultant exchange interactions. Dielectric

constants in the range 5-7 and permeability in the range 2-6 make this ferrite very useful in microwave devices and as a potential EMI shielding material [37].

In the work of Silvana Da Dalt *et.al.,* they obtained the phase $BaFe_2O_4$ at low temperature (600℃) from the combustion reaction using nitrates and maleic anhydride as metal complexing agents. For the samples subjected to heat treatment at temperatures below 1000℃ secondary phases of low crystallinity were observed. This affects the photocatalytic activity of these samples. Samples annealed at 900 and 1000℃ showed considerable photocatalytic activity because of well-defined crystalline phases and high surface areas [38].

Samira Mandizadeh synthesized $BaFe_2O_4$ nanostructures by hydrothermal method using PTSA (p-toluene sulfonic acid) as fuel. Samples were prepared at 800℃, 900℃ and 1000℃. From SEM images of the sample the best PTSA: $Ba(NO_3)_2$ ratio for uniform particle size is 3:1. Also the mean particle size increases with an increase in calcination temperature. An orthorhombic phase formation was found to be at 1000℃. The crystallinity was found to increase with increasing calcination temperature. Magnetic properties by VSM show that the minimum grain diameter for maximum coercivity is 0.1μm for Ba-ferrite[39].

The structure and magnetic properties of nanosized $BaFe_2O_4$ were studied by Adnan Jaafar *et. al.,* A mixture of BaO and Fe_2O_3 was mechanically alloyed followed by annealing up to 900℃ to form the $BaFe_2O_4$ phase and some $BaFe_{12}O_{19}$ phase. The temperature rise causes a dramatic change in the magnetic properties, especially the coercivity Hc = 1.2kOe which reflects the achievement of nanoscale domains [40].

In the study of Reza Peymanfar prepared $BaFe_2O_4$ spinel structures through a sol-gel route using a low sintering temperature. When the calcination temperature increases from 450 to 650℃ phase pure $BaFe_2O_4$ was obtained. The FTIR curve demonstrated that the metal-oxide bonds of $BaFe_2O_4$ nanoparticles had been synthesized at a low temperature. $BaFe_2O_4$/silicone rubber nanocomposite with 1.75 mm thickness absorbed more than 94.38% of microwave irradiation at the Ku-band frequency, and the maximum reflection loss of the $BaFe_2O_4$/silicon rubber nanocomposite was 51.67 dB at 16.1 GHz. The result suggests that $BaFe_2O_4$ nanoparticles can be a promising microwave absorbing material [41].

Abdollah Javidan *et al* synthesize $BaFe_2O_4$ using a novel precursor barium oxalate (BaC_2O_4) by thermal decomposition process without using any surfactants or additives. Pure $BaFe_2O_4$ samples were obtained by calcinating at 800℃ for 2 hours in a gas mixture of 85% Ar and 15% H_2. Saturation magnetization, remanent magnetization and coercivity of the $BaFe_2O_4$ were 15.5emu/g, and 2500 Oe respectively [42].

1.9 Motivation for the present study

Material science is all about developing new materials or improving the properties of existing materials having potential applications in various fields like magnetism, electricity, energy storage and wastewater treatment. Recently, material science researchers focused on multiferroic materials in which the material exhibit magnetism and ferroelectricity in a single phase at room temperature. Last few years, a lot of families like manganites, chromites and ferrites have been identified as multiferroic. Multiferroic materials can satisfy the demand of future technology by giving much smaller, faster and energy-efficient data storage devices for various purposes.

From recently developed multiferroic materials, ferrites have great attention due to the exhibition of multiferroic properties at room temperature. In these, $BiFeO_3$ is a well-known ferrite which exhibits both ferromagnetism and ferroelectricity at room temperature. Due to the difficulties of synthesizing conditions in $BiFeO_3$, multiferroics studies in ferrites have been spread out to different families. Consequently, Ferrites with the general formula $M^{2+}\,Fe_2^{3+}O_4$ (M is a divalent metal ion) have keen interest due to its ferromagnetic behaviour at room temperature. Its high saturation magnetization and high coercivity properties are exploited to use as permanent magnets in recording media where materials need to be able to withstand strong demagnetizing forces. Considering the electrical properties ferrites are semiconductors or insulators in a contrast to metallic magnetic materials that are electrical conductors. Hence, they possess high intrinsic resistivity which limited the eddy currents loss in these ferrites. Besides these properties, they also exhibit high curie temperature, greater chemical stability, greater heat resistance and higher corrosion resistance [43–46].

Most of the MFe_2O_4 explored to date transition metals are used in M sites due to the localized 3d electrons in the valence which are usually magnetic if they are unpaired. Also, the bond between the transition metal and oxygen in spinel ferrites is neither too ionic nor too covalent which makes them easily polarizable. These two properties are

favourable for inducing ferromagnetism and ferroelectricity respectively in the system. In transition metal ferrites, cobalt ferrite ($CoFe_2O_4$) is a better choice for many practical applications as it exhibits chemical stability, large coercive field, large magnetization, low dielectric loss and eddy current at room temperature. The larger magnetic moment of Co^{2+} and Fe^{3+} ions are the reason for the exhibition of ferrimagnetism with large magnetization at room temperature. Cobalt ferrites show a mixed spinel structure where both Co^{2+} and Fe^{3+} are occupied in both octahedral and tetrahedral sites [32,33]. A small distortion in octahedral and tetrahedral sites created through the synthesis method or inclusion of foreign atoms affects the centrosymmetricity of the entire system which could be favourable to induce ferroelectricity.

Recently, It is observed that alkaline earth metals are a replacement for transition metals in ferrites which gives higher ferroelectric and ferromagnetic properties at room temperature. For example, $SrFe_{12}O_{19}$ is already used in electric vehicles and $BaFe_{12}O_{19}$ is widely studied to introduce in technological areas. In MFe_2O_4, Barium Monoferrite ($BaFe_2O_4$) is a less studied material due to the difficulty in getting it as a single phase due to the coexistence of a strong phase, Barium Hexaferrite ($BaFe_{12}O_{19}$) along with the Fe_2O_3. $BaFe_2O_4$ has an orthorhombic structure where the Fe^{3+} is bonded tetrahedrally with O^{2-} cations which are very interesting to further studying the crystal structure and phase formation [30]. $BaFe_2O_4$ has several advantages compared to other MFe_2O_4 ferrites such as the high capacity of magnetization, high coercivity, highly stable, high permittivity, and low band gap. Due to the low band gap properties, Barium Monoferrite is used as an important candidate for visible light photo-catalysis and as a ceramic pigment [38]. Another beneficial property of $BaFe_2O_4$ such as high permittivity is rarely studied. There are no detailed studies on the magnetic and microwave properties of $BaFe_2O_4$. The developments of microwave and radar absorber materials (M-RAM) are growing rapidly to be applied in military applications and information technology. As the candidate material which would be applied as M-RAM material should have high permittivity and permeability values, the high permittivity behaviour of $BaFe_2O_4$ will make this ferrite material a good candidate to be applied as MRAM material.

The proposed work is a comparative study between $BaFe_2O_4$ and $CoFe_2O_4$ in their structural, optical, magnetic and dielectric properties at room temperature. Successful

completion of this project will help to develop efficient devices with these materials for military applications and information technology.

Chapter 2
Synthesis and Characterization Techniques

2.1 Synthesis Method

Ferrite materials can be synthesized by a variety of methods such as the Co-precipitation method, Sol-gel method, Combustion method, Hydrothermal method etc. Structural, electrical, dielectric and magnetic properties of ferrites have a strong dependence on the preparation methods. Desirable properties of ferrite materials can be obtained by using suitable methods. Sol-gel method has a lot of advantages over other synthesis methods. It has proven to be quite promising to obtain nanostructured ferrite powders. The following section discusses the sol-gel method.

2.1.1 Sol-gel Method

The sol-gel method is a bottom-up approach in which atomic level particles is converted to particles of size 1-100nm. It is a wet chemical method for the synthesis of various nanomaterials, especially metal oxide nanoparticles. In the sol-gel method sample to be synthesized must pass through two phases ‘sol’ and ‘gel’. Sol means colloidal suspension in a solvent. The colloidal sol is prepared using the chemicals in which metals or metalloids are surrounded by ligands, e g: nitrates of corresponding metals. In the synthesis of systems containing more than one cation, the entrapment of cations in a polymer network is an effective method to avoid the formation of multiple phases of binary oxides as the result of differences in hydrolysis and condensation rates. This method is termed as Pechini Process in which a chelating agent is used, most often citric acid to surround aqueous cations and sterically entrap them. An aqueous solution of metal nitrate and citric acid is made using deionized water. This undergoes hydrolysis in which the hydroxyl ion is attached to the metal ion. Then it is placed on a hot plate providing the necessary heat. Then condensation reaction takes place and produces a larger metal-containing molecule through the process of polymerization. As the molecule reaches macroscopic dimensions extending throughout the solution the substance formed is termed ‘gel’. Thus gel is a stage of substance which contains a continuous solid structure enclosed in a continuous liquid phase that possesses elasticity. The formation of a polymer network to immobilize the chelated cation in the

gel is achieved by polyesterification using ethylene glycol. As the heating continues the gel began frothing after the evaporation of all the water molecules from the mixture. In the later stage, the gel is automatically ignited and decomposition takes place till the consumption of the whole of the fuels. After the ignition brown coloured ashes are obtained [47].

After the synthesis, we do a post-synthesis treatment called sintering. Sintering means materials heated at a high temperature and it will help to distribute grains periodically.

Sol-gel is very simple and economical, most importantly it requires a low temperature that keeps the characteristics of the powder like purity, chemical homogeneity, shape and size of the particle as much under control. It needs only a simple compound and does not require any special equipment, doping can be easily introduced and the agglomeration of powders remains limited [47].

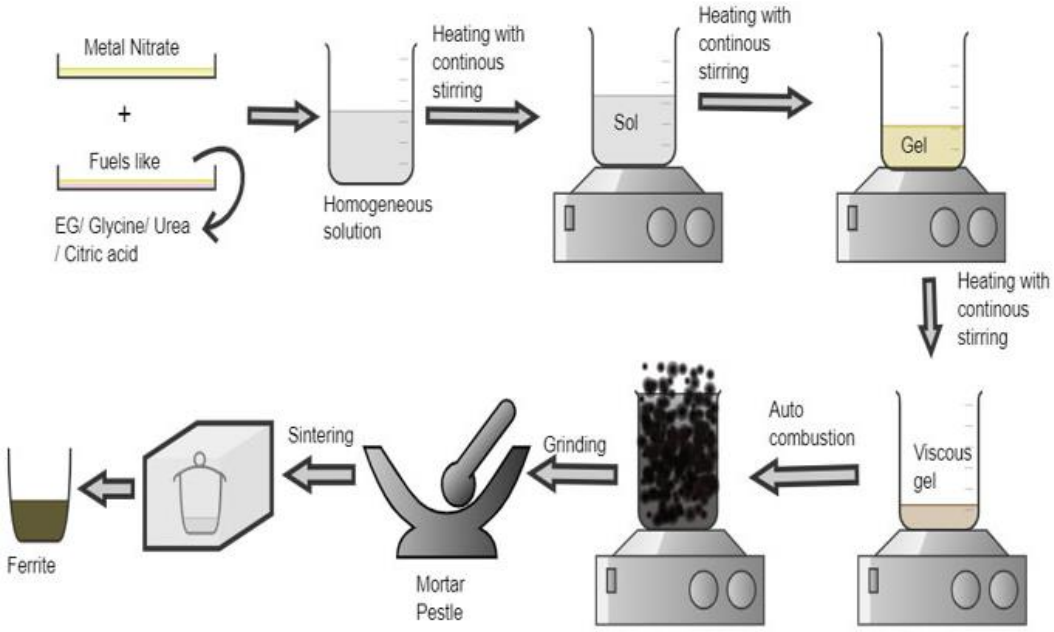

Figure 2.1 Different steps in sol-gel method [48]

2.2 Characterization techniques

To study the structural, electrical, magnetic, optical and many other properties of materials different characterization techniques are used. This section describes the theory and working principle of these characterization techniques and how it is useful to understand the properties of desired materials.

2.2.1 X-ray Diffraction Technique (XRD)

X-ray diffraction is a characterization technique used to study the structure of materials. It is used to determine the crystal structure and lattice parameters of a material system. X-ray diffraction peaks are produced by constructive interference of a monochromatic beam of X-rays diffracted at specific angles from each set of lattice planes in a crystal [49].

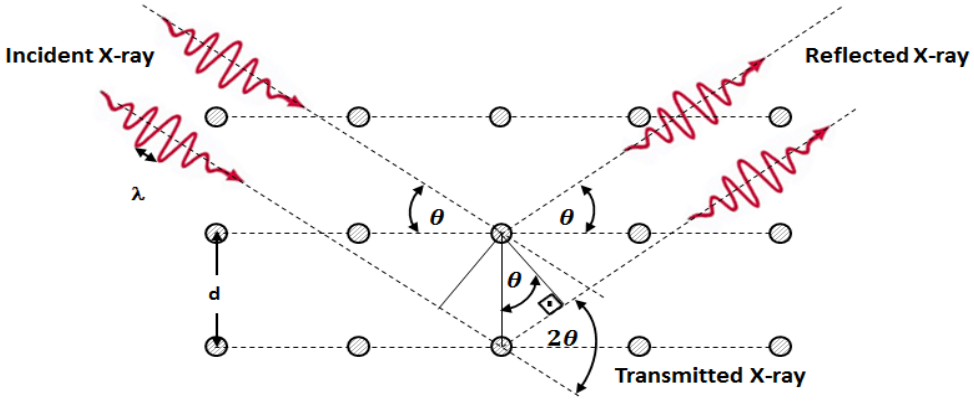

Figure 2.2 Schematic diagram of Bragg's law [50]

Diffraction peaks occur only when Bragg's law is satisfied $n\lambda = 2d\sin\theta$, where d is the inter-planar distance between crystalline planes, λ is the wavelength of X-ray used, and n is the order of diffraction and θ is the angle of incidence.

An X-ray diffractometer consists of three basic elements: X-ray tube, sample holder and X-ray detector. X-rays are produced in the cathode ray tube. These X-rays are collimated and directed into the sample. According to the geometry of the diffractometer, the sample rotates in the path of the collimated X-ray beam at an angle of θ while the X-ray detector is mounted on an arm to collect the diffracted X-rays and rotates at an angle of 2θ [49].

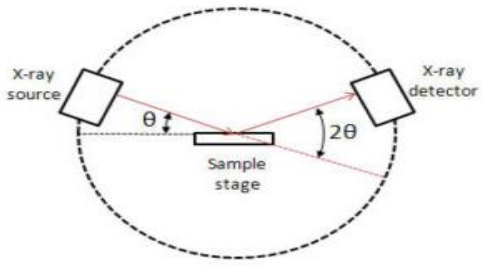

Figure 2.3 Schematic diagram of an X-ray diffractometer [51]

X-ray diffraction pattern plots the intensity of diffracted x-rays versus 2θ. Peak position 2θ provides information on lattice parameters, symmetry, shape and size of the unit cell. Peak intensity depends on the type of molecule and the number of planes. The width and shape of the peak depending on the crystallite size and defects like strain and disorder.

Debye Scherrer equation relates the crystallite size to the broadening of the diffraction peak and is given by,

$$D = \frac{K\lambda}{\beta\cos\theta} \qquad (9)$$

where D is volume-weighted crystallite size, K is Scherrer constant its value ranges 0.87-1.0, β is full-width half maximum of diffraction peak.

2.2.1.1 Rietveld Refinement

Although crystal structure determination from powder diffraction data is simple in theory, it is highly challenging in the case of multiphase analysis due to overlapped reflections. The Rietveld method is used to refine the crystal structure of a material and obtain accurate structural parameters of the different phases in the sample under investigation. It refines the user-selected parameters to minimize the difference between an experimental pattern (observed data) and a model based on the hypothesized crystal structure and instrumental parameters (calculated pattern). Common parameters refined when fitting the data include structural parameters (the unit cell parameters, fractional atomic coordinates, atomic site occupancies and atomic displacement parameters), parameters describing the instrument calibration (e.g: any 2θ zero-pint offset), parameters describing any 2θ-dependent intensity correction (e.g: due to absorption), parameters describing peak shape, and parameters describing the background between the Bragg peaks. In refinement, we try to minimize the difference between observed diffraction intensity and calculated intensity at each step in 2θby changing certain parameters. It is given by

$$\sum_{i=1}^{N} w_i(y_{i(obs)}-y_{i(calc)})^2. \qquad (10)$$

Peaks in an XRD pattern are a mixture of Gaussian and Lorentzian functions. To obtain the best fit w use the pseudo-Voigt function which is the sum of Lorentzian and Gaussian profiles. The formulation for FWHM with angular dependence is given by

$$(FWHM)_k = U\tan^2\theta_k + V\tan\theta_k + W \qquad (11)$$

U, V, and W are adjustable parameters. Refinement of these parameters gives a good fit [52].

2.2.2 UV-Visible Spectroscopy

VU-Visible spectroscopy investigates the optical properties of materials. It is a quantitative measurement of the absorption/transmission or reflection of light by a material as a function of wavelength. Generally, UV-Visible spectrometers are used in a wavelength region of 190-900 nm.

The spectrometer consists of a source lamp which can be a xenon lamp, tungsten, halogen or a deuterium lamp, and a monochromator which is two slits separated by a prism or diffraction grating. The first slit ensures that all the light is travelling on parallel pathways. When it is passed through a prism or grating refraction occurs which splits the light into its constituent colours. Thus only one wavelength of light passes through the second slit. The next part is a beam splitter which divides the light beam into two equal parallel beams of light that are allowed to pass through the sample cell and the reference cell. Then the detectors convert light into electrical current that can be monitored by a computer [53].

A UV-Visible spectrometer measures the amount of light transmitted through a sample by rationing the intensity of the incident light (I_0) to the intensity of the transmitted light (I). The relation between transmittance (T) and absorbance (A) is given by,

$$A = -\log T \qquad (12) \qquad \text{where } T = I/I_0$$

UV-Visible spectroscopy is used for solid and liquid samples. For solids, we determine the reflectance of the material. This UV-Visible spectroscopy is also called diffuse reflectance spectroscopy. The optical absorption coefficient can be calculated from the reflectance data by using the Kubelka-Munk function,

$$\alpha = (1-R)^2/2R \qquad (13) \qquad \text{where R is the diffuse reflectance.}$$

The optical band gap is determined using the Tauc relation

$$(\alpha h\nu) = A\,(h\nu - Eg)^n \qquad (14)$$

A is a constant, Eg is the energy gap, hν is the energy of the incident photon, and n is an index that characterizes the optical absorption process [53].

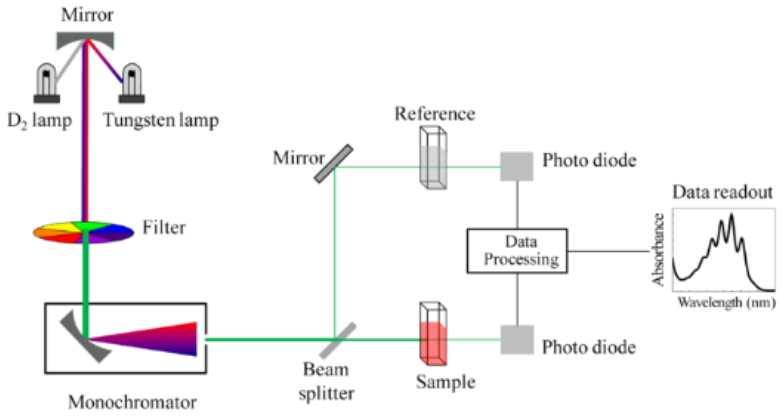

Figure 2.4 Schematic diagram of UV Visible Spectrophotometer [54]

2.2.3 Dielectric spectroscopy

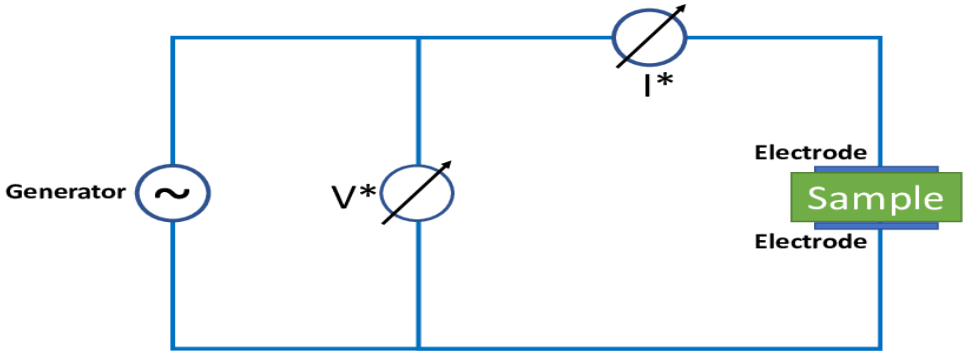

Figure 2.5 Schematics of dielectric measurements [55]

Dielectric spectroscopy measures the dielectric properties of a medium as a function of frequency or time. It is also known as Impedance Spectroscopy. It is based on the interaction of an external field with the electric dipole moment of the sample, often expressed by the permittivity. This technique measures the impedance of a system over a range of frequencies, and so the frequency response of the system including the energy storage and dissipation properties is revealed. In impedance spectroscopy sample is placed between two electrodes and a known voltage is applied. The resulting current and voltage are measured by varying parameters like frequency, the temperature of the sample, pressure, current bias etc. The electric field can be applied to the sample in three ways. The output obtained in the form of the current can be converted into

frequency-dependent data by Fourier or Laplace transform. The method of applying single frequency current or voltage into the sample and measuring capacitance, phase or impedance of the sample is the standard method used for research purposes. Dielectric spectroscopy gives information on important material parameters such as static dielectric permittivity (ε) and DC electrical conductivity (σ). It is also used to evaluate the dielectric properties such as dielectric constant, dielectric loss etc [56].

2.2.4 Vibrational sample magnetometer (VSM)

A vibrating sample magnetometer or VSM is a scientific instrument to measure magnetic properties. It operates on Faraday's Law of induction, according to which a changing magnetic field produces an electric field. This electric field provides information about changing magnetic fields. VSM operates by placing the sample to be studied in a constant magnetic field. This field magnetizes the sample if it is magnetic and creates a magnetic field around it. As the sample is moved up and down, this magnetic field changing as a function of time can be sensed by a set of pick-up coils. The changing magnetic field produces an electric field in the coils. This current will be proportional to the magnetization of the sample. The induction current is amplified by a trans-impedance amplifier and lock-in amplifier. The various components are connected to a computer interface. Using controlling and monitoring software, the degree of magnetization of the sample and the dependence of magnetization on the strength of the constant magnetic field can be determined [57–59].

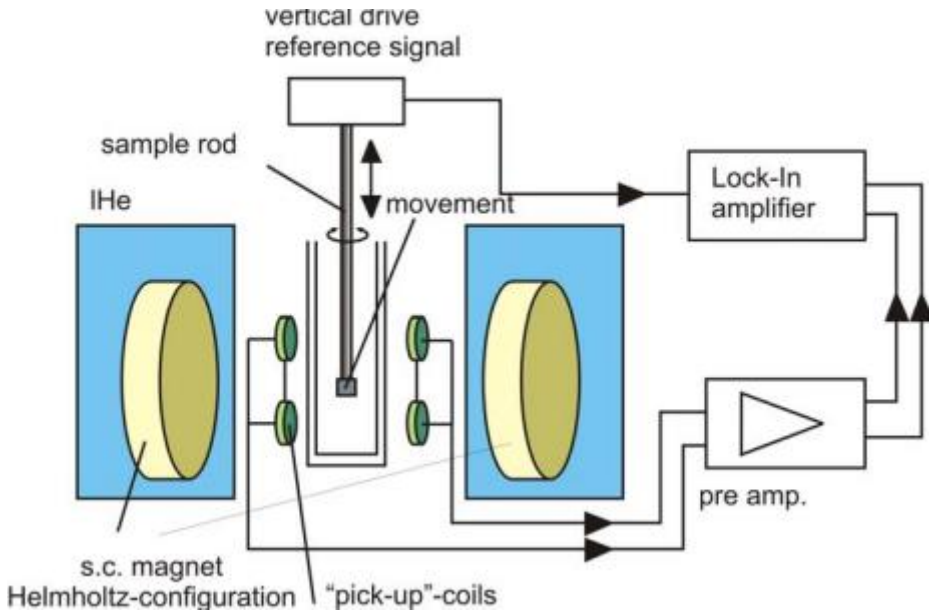

Figure 2.6 Schematic diagram of vibrating sample magnetometer [60]

Chapter 3
Results and Discussion

3. 1. Preparation and Characterization of $CoFe_2O_4$ and $BaFe_2O_4$

3.1.1 Synthesis of $CoFe_2O_4$

Single phasic $CoFe_2O_4$ powders are successfully synthesized through glycine assisted sol-gel method. Cobalt nitrate and iron nitrate are taken as the salt precursors for the synthesis of $CoFe_2O_4$. Stoichiometric amounts of $Co(NO_3)_2.6H_2O$ and $Fe(NO_3)_3.9H_2O$ are taken to prepare solutions which contain Co and Fe ions. Nitrates in Co and Fe ions are dissolved in DM water. These cation solutions are mixed with glycine solution which acts as fuel. The resultant solution is stirred well at 80º C for 30 minutes to obtain a homogeneous solution. The resultant solution is heated at a temperature of around 250ºC using a hot plate until all the solvents evaporated from the resultant solution. After a few hours, the solution gets boiled, frothed, turned dark, then ignited and caught fire to give a spongy powder. The resultant powder is ground thoroughly using mortar and pestle. The resulting black-coloured powder is sintered at 800ºC for 5 hours in a high-temperature furnace.

3.1.2 Synthesis of $BaFe_2O_4$

Barium Ferrite ($BaFe_2O_4$) is prepared by the citric acid-assisted Sol-gel method. Barium Ferrite is prepared using Barium Nitrate $Ba(NO_3)_2$ and Iron Nitrate $Fe(NO_3)_3$ as the starting materials, citric acid and ethylene glycol as fuels. The required weight of the metal salts is weighed separately and dissolved in distilled water. Then the solutions of Barium Nitrate and Iron nitrate are added to an aqueous citric acid solution with the appropriate amount of ethylene glycol. To make a perfect homogeneous solution, it is mixed using a magnetic stirrer for 30 minutes at 80^0 C. Then the solution is placed on a hot plate at around 250^0 C until a dry gel is obtained. Then it is grounded well using an agate mortar. The powder is sintered in a furnace for 5 hours at 1300^0C for densification. After this process, the powder is again grounded.

3.1.3 Characterization of $CoFe_2O_4$ and $BaFe_2O_4$

The crystal structure of the $CoFe_2O_4$ and $BaFe_2O_4$ is determined by a Bruker X-ray diffractometer with Cu Kα X-ray radiation of a wavelength of 1.5406 Å. Quantum Design MPMS3 magnetometer is used to study the room temperature magnetic properties of $CoFe_2O_4$ and $BaFe_2O_4$ The powders obtained from the sol-gel method were pelletized into circular discs and they are used to study the dielectric properties at room temperature by HIOKI IM 3570 impedance analyzer. The absorbance spectrum of $CoFe_2O_4$ and $BaFe_2O_4$ are carried out by a JASCO 750 UV-Visible spectrophotometer in the wavelength range of 250-800 nm.

3. 2. Structural Studies

The Qualx software is used to identify the structure of MFe_2O_4 (M- Co, Ba) and to check whether or not any impurity peaks are present. The Qualx software, a computer program, can identify crystal phases by powder X-ray diffraction data. It is based on the traditional search–match approach and is characterized by a high level of automatism and a user-friendly graphic interface. More importantly, this software is free and is easily available for any students and researchers

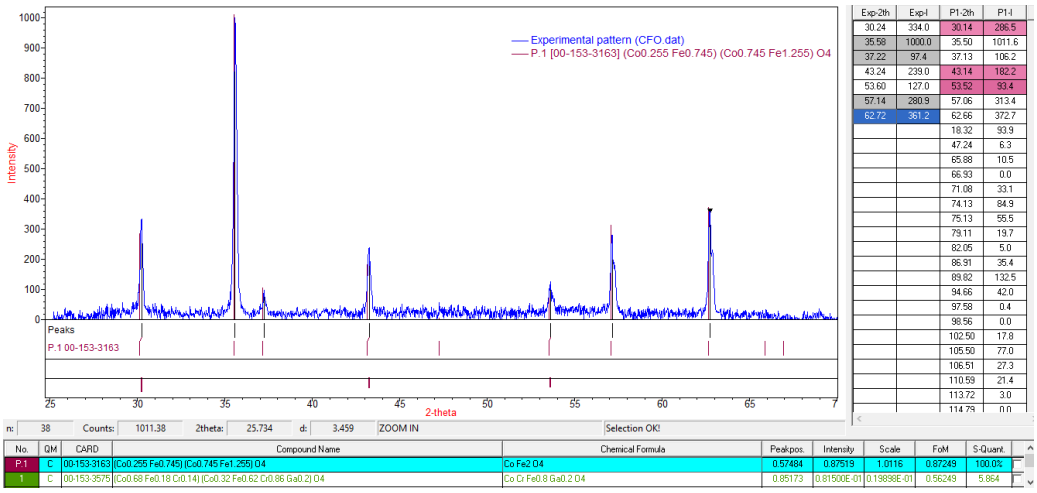

Figure 3.1 XRD pattern of $CoFe_2O_4$ with reported XRD patterns by Qualx software

Figure 3.1 and 3.2 shows the XRD pattern of $CoFe_2O_4$ and $BaFe_2O_4$ with some earlier reported XRD patterns by Qualx software. It is found that the XRD pattern of $CoFe_2O_4$ is matched with COD ID: 000-153-3163 with a figure of merit of 0.87249 and $BaFe_2O_4$ matched with COD ID: 000-430-9915 with a figure of merit 0.79193. The Figure of merit indicates how much the reported value matched with experimental data.

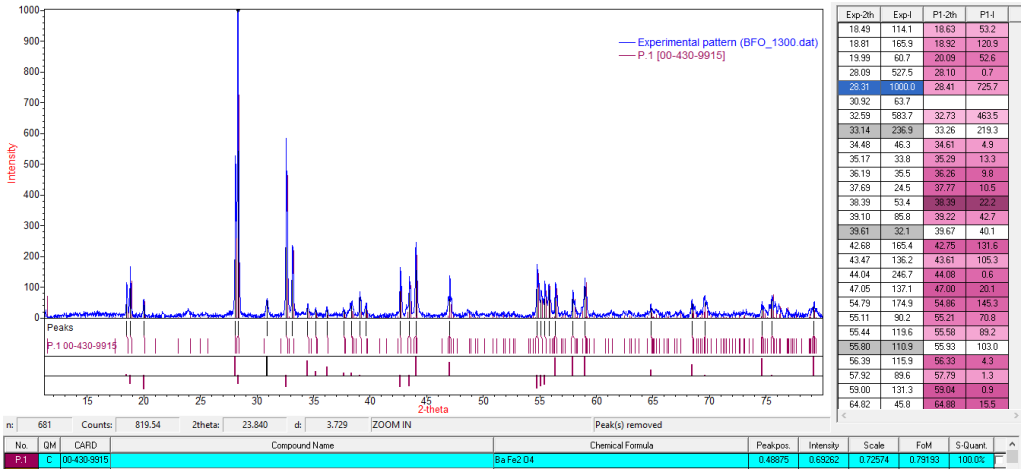

Figure 3.2 XRD pattern of $BaFe_2O_4$ with reported XRD patterns by Qualx software

Figure 3.3 and 3.4 show the card information of COD ID: 000-153-3163 and 000-430-9915. From the database, It is seen that $CoFe_2O_4$ exhibits a mixed spinel cubic structure with a space group Fd-3m and $BaFe_2O_4$ exhibits an orthorhombic structure with a space group $Cmc2_1$.

00-153-3163

COD CIF File	http://www.crystallography.net/cod/1533163.html
Name	(Co0.255 Fe0.745) (Co0.745 Fe1.255) O4
Formula	Co Fe2 O4
Quality	C (calculated pattern)
I/Ic	6.05
Reference	Ferreira, T.A.S. Waerenborgh, J.C. Mendonca, M.H.R.M. Costa, F.M. Nunes, M.R., Solid State Sciences, **5** (2003)
Space Group	F d -3 m :2 (227)
Crystal system	Cubic
Cell parameters	a=8.3806 Å
Cell volume	588.61 Å3
Z	8
Wavelength	1.54056 Å
μ(Cu Kα)	1206.167 cm-1

Diffraction data

2theta	d[A]	Int.	hkl	mult
18.3207	4.8385	92.84	1 1 1	8
30.1361	2.9630	283.21	2 2 0	12
35.4976	2.5268	1000.00	3 1 1	24
37.1311	2.4193	104.99	2 2 2	8
43.1425	2.0951	180.17	4 0 0	6
47.2370	1.9226	6.18	3 3 1	24
53.5222	1.7107	92.35	4 2 2	24
57.0581	1.6128	309.84	5 1 1	24
62.6554	1.4815	368.49	4 4 0	12

Figure 3.3 Card information of COD ID: 000-153-3163

00-430-9915

COD CIF File	http://www.crystallography.net/cod/4309915.html
Formula	Ba Fe2 O4
Quality	C (calculated pattern)
I/Ic	5.95
Reference	Pavel Karen Emmanuelle Suard Fran,cois Fauth, Inorganic Chemistry, **44** (2005)
Space Group	C m c 21 (36)
Crystal system	Orthorhombic
Cell parameters	a=8.4538 Å b=19.0400 Å c=5.3826 Å
Cell volume	866.39 Å3
Z	8
Wavelength	1.54056 Å
μ(Cu Kα)	1210.414 cm-1

Diffraction data

2theta	d[A]	Int.	hkl	mult
9.2820	9.5200	0.18	0 2 0	2
11.4432	7.7264	97.15	1 1 0	4
17.4584	5.0755	3.29	1 3 0	4
18.6255	4.7600	73.36	0 4 0	2
18.9244	4.6855	166.56	0 2 1	4
20.0886	4.4165	72.53	1 1 1	8

Figure 3.4 card information of COD ID: 000-430-9915

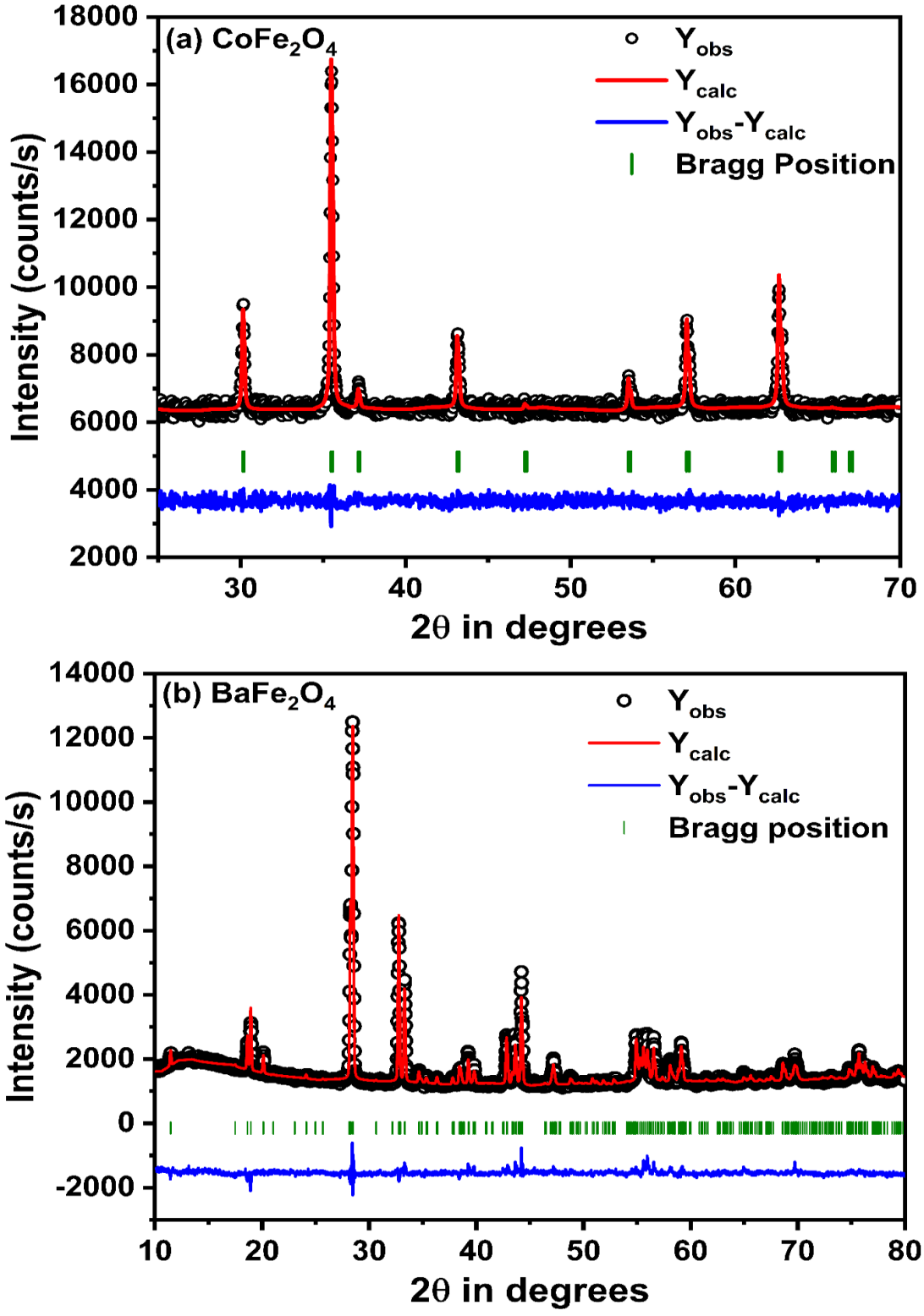

Figure 3.5 Rietveld refined XRD patterns of (a) $CoFe_2O_4$ and (b) $BaFe_2O_4$

To get the complete picture of crystal structure and cation distribution of $CoFe_2O_4$ and $BaFe_2O_4$, Rietveld refinement analysis of XRD patterns of $CoFe_2O_4$ and $BaFe_2O_4$ is

carried out using FULLPROF software and it is shown in Figure 3.5. The properties of crystal structure and space group are summarized in table 3.1. It is observed that $CoFe_2O_4$ exhibit a centrosymmetric structure having two origins from octahedral and tetrahedral sites. Hence, the distortion occurred in either octahedral or tetrahedral sites can induces spontaneous polarization and thereby exhibits ferroelectric nature in $CoFe_2O_4$. Still, due to the overall centrosymmetric nature of $CoFe_2O_4$ crystal, it exhibits only an improper ferroelectricity at room temperature. However, from refinement, it is revealed that $BaFe_2O_4$ have a non-centrosymmetric crystal structure and due to this acentric nature $BaFe_2O_4$ can induce high spontaneous polarization with proper ferroelectricity and it is already reported. The refined lattice parameters, atomic positions and occupancies of both $CoFe_2O_4$ and $BaFe_2O_4$ are summarized in tables 3.1 and 3.2. It is observed that $BaFe_2O_4$ have a larger cell volume than $CoFe_2O_4$ due to the larger ionic radii of Ba (1.35 Å) ions than Co (0.745 Å) ions.

Table 3.1 Detailed information on the crystal structure

Detailed information on Crystal Structure		
Crystal structure and space group		
	$CoFe_2O_4$	$BaFe_2O_4$
Crystal Structure	Cubic	Orthorhombic
Space group	Fd-3m	$Cmc2_1$
Laue class	mmm	m-3m
Centrosymmetry	Centric	Acentric
Cell parameters (Å)	a=b=c= 8.3826	a = 8.4420 b = 19.0395 c = 5.3800
Cell Volume ($Å^3$)	589.0223	864.7310
Density (g/cm^3)	5.291	4.771

Refined atomic positions and occupancies of $CoFe_2O_4$ and $BaFe_2O_4$ are tabulated in table 3.2. In $CoFe_2O_4$, both Co ions and Fe ions are situated in octahedral and tetrahedral sites surrounded by oxygen atoms. Meanwhile, in $BaFe_2O_4$, Ba ions are situated in dodecahedral and Fe ions are situated in tetrahedral sites surrounded by oxygen atoms. From atomic positions, it is revealed that the oxygen ion positions of

$CoFe_2O_4$ get shifted which causes the structural distortion in the material. However, in BaFe2O4, Barium, iron and oxygen atoms positions simultaneously shifted and it equally contributes to the structural distortion. Therefore the structural distortion occurred by defects and induced strain can affect more in $BaFe_2O_4$ system than in $CoFe_2O_4$. With the help of these Wyckoff positions and occupancies, the crystal structure of both $CoFe_2O_4$ and $BaFe_2O_4$ are visualised in figure 3.6.

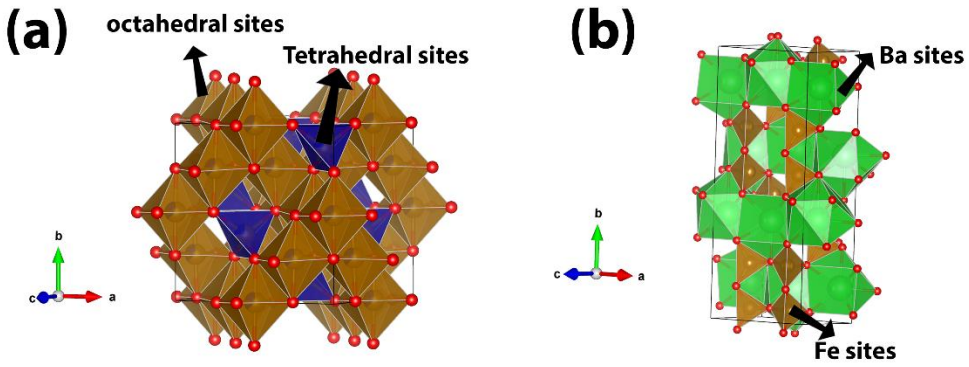

Figure 3.6 Crystal structure of (a) $CoFe_2O_4$ and (b) $BaFe_2O_4$

Table 3.2 Refined atomic positions and occupancies of $CoFe_2O_4$ and $BaFe_2O_4$

Compound	Atoms	Atomic positions			Occupancy
		x	y	z	
$CoFe_2O_4$	Co (T)	0.1250	0.1250	0.1250	0.01162
	Co (O)	0.5000	0.5000	0.5000	0.03004
	Fe (T)	0.1250	0.1250	0.1250	0.03105
	Fe (O)	0.5000	0.5000	0.5000	0.05228
	O	0.2452	0.2452	0.2452	0.16667
$BaFe_2O_4$	Ba (1)	0.0000	0.1303	0.4542	0.5040
	Ba (2)	0.0000	0.6185	0.4455	0.4960
	Fe (1)	0.2802	0.0418	0.9240	1.0039
	Fe (2)	0.2906	0.2064	0.9548	0.9961
	O (1)	0.2024	0.0285	0.5488	1.0000
	O (2)	0.2248	0.1147	1.0813	1.0000
	O (3)	0.2617	0.2097	0.6450	1.0000
	O (4)	0.0000	0.4310	0.4738	0.5000
	O (5)	0.0000	0.2306	0.1837	0.5000

Williamson Hall method is employed to study the crystallite size and induced strain in $CoFe_2O_4$ and $BaFe_2O_4$ material. According to the W-H method, the line broadening occurred in XRD patterns due to the influence of the crystallite size of the lattice and induced strain in the lattice is expressed as [61].

$$\beta cos\theta = \frac{k\lambda}{D} + \varepsilon 4 sin\theta \qquad (15)$$

Here β is the full-width half maximum of characteristic peaks in radians, θ is the position of characteristic peaks in degree, D is the crystallite size of the material and ε is the induced strain in the material. The graph between 4sinθ with βcosθ for $CoFe_2O_4$ and $BaFe_2O_4$ is shown in figure 3.7. The intercept of the line gives the corrected crystallite size, and the slope gives the type and magnitude of the strain induced in the lattice. $CoFe_2O_4$ exhibit a negative slope which denotes that the strain induced in the material is compressive. $BaFe_2O_4$ exhibit a positive slope indicating the existence of tensile strain. Comparing the magnitude of the strain, $CoFe_2O_4$ have a large induced strain. The Crystallite size of $CoFe_2O_4$ and $BaFe_2O_4$ is 57 nm and 60 nm respectively.

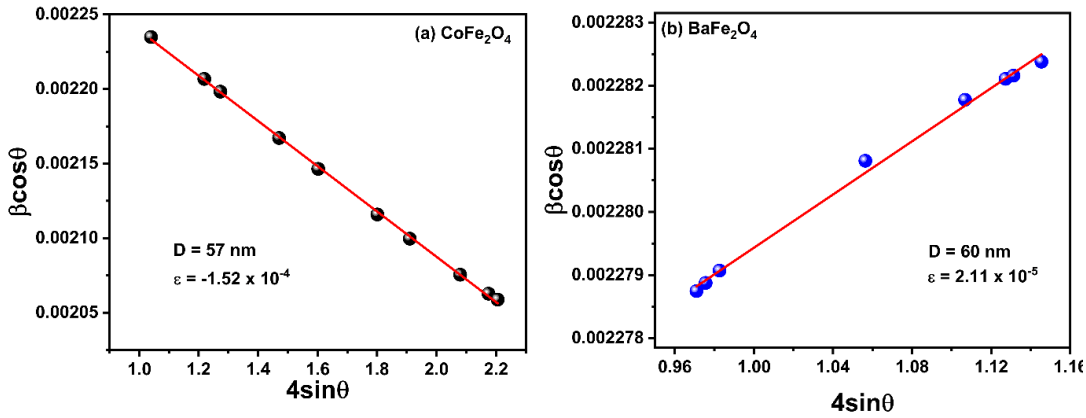

Figure 3.7 W-H plot of (a) $CoFe_2O_4$ and (b) $BaFe_2O_4$

3.3 Magnetic Studies

Figure 3.8 shows the isothermal magnetic hysteresis curve of $CoFe_2O_4$ and $BaFe_2O_4$ at room temperature. It is found that, $CoFe_2O_4$ exhibit a ferrimagnetic behaviour with a well-saturated hysteresis curve having magnetic saturation ~88 emu/g. However, in $BaFe_2O_4$ samples, magnetic saturation is not obtained even in an applied field of 70 KOe having a maximum magnetization ~2.0 emu/g. This unsaturated magnetization is mainly due to the coexistence of ferrimagnetism and weak antiferromagnetism. From the figure, it is observed that the magnetization of $BaFe_2O_4$ is lower than $CoFe_2O_4$. In ferrites, Fe ions are the major source of magnetism due to its high value of magnetic

moment. Besides Fe, Ba and Co ions also have a minor contribution to induce magnetism in $BaFe_2O_4$ and $CoFe_2O_4$ respectively. From the theoretical calculation, Ba and Co have the magnetic moment of 0 μ_B and ~3.87 μ_B respectively. Due to this zero magnetic moment of Ba ions, $BaFe_2O_4$ shows a small magnetization. Besides saturation magnetization, coercivity and remanent magnetization have an important role to develop efficient permanent magnets, recording devices and memory devices. The magnetic domain structures of each ferrites are different based on the magnetic moment of cations and cation distribution in the system, this difference will influence the coercivity and remanent magnetization. Coercivity and remanent magnetization of $CoFe_2O_4$ and $BaFe_2O_4$ are tabulated in table 3.3. From the table, It is found that $BaFe_2O_4$ have higher coercivity than $CoFe_2O_4$. This variation of coercivity depends on the magnetocrystalline anisotropy occurred in the systems. Magnetocrystalline anisotropy is defined as the energy needed by the material to align the magnetic moment from the easy axis to the hard axis in the presence of the external field.

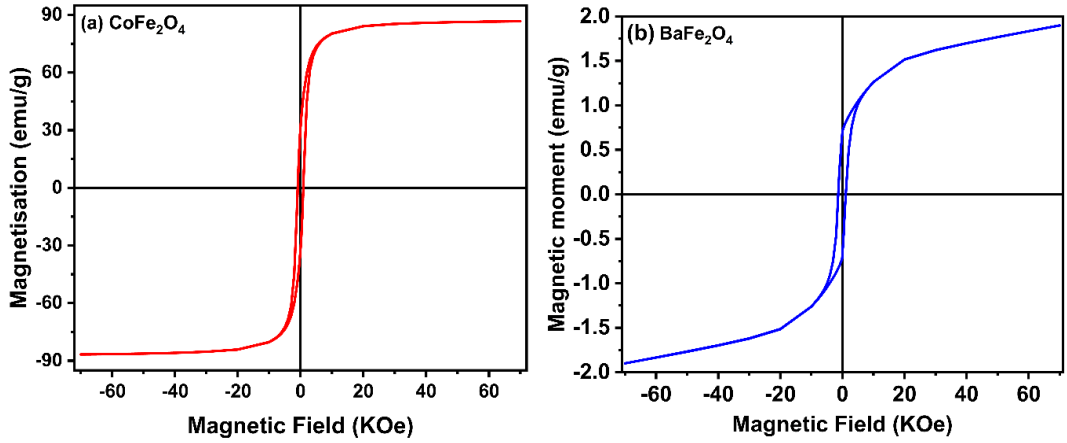

Figure 3.8 Magnetic hysteresis curve of (a) $CoFe_2O_4$ and (b) $BaFe_2O_4$

Table 3.3 Saturation magnetization, Coercivity and remanent magnetization of $CoFe_2O_4$ and $BaFe_2O_4$

Compound	M at 70 KOe	Coercivity (Oe)	Remanence (emu/g)
$CoFe_2O_4$	86.73	888	31.48
$BaFe_2O_4$	1.90	1073	0.70

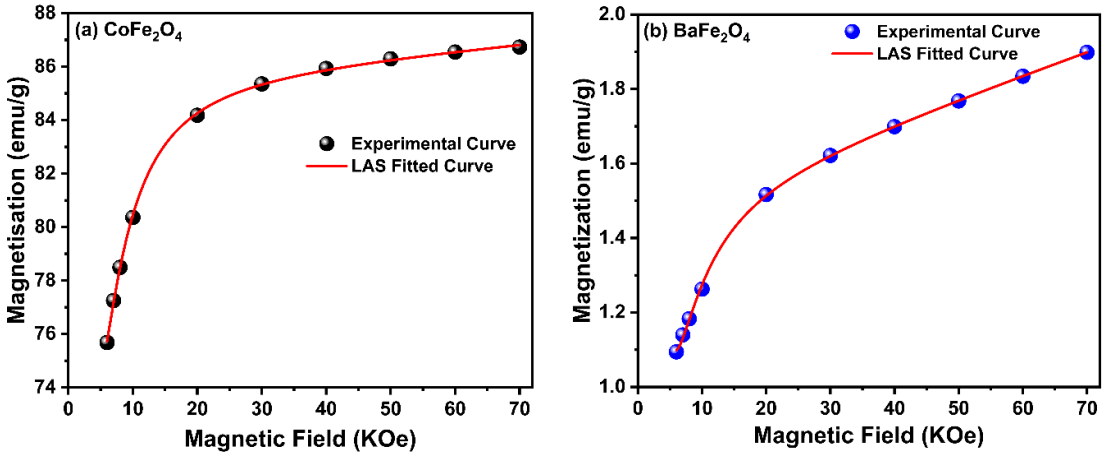

Figure 3.9 LAS Fittinfg of (a) $CoFe_2O_4$ and (b) $BaFe_2O_4$ at higher applied fields

To deduce the effect of magneto crystalline anisotropy in $CoFe_2O_4$ and $BaFe_2O_4$, the curve corresponding to magnetization with respect to the higher magnetic field is fitted by the Law of Approach to saturation (LAS). The equation of LAS is expressed as [62–64],

$$M = M_s\left(1 - \frac{a}{H} - \frac{b}{H^2} - \frac{c}{H^3}\right) + \chi H \qquad (16)$$

Where M_s represents the saturation magnetization of the material, 'a' represents the inhomogeneity parameter which explains the effect of induced strain, defects and non-magnetic ions in the material. The third and fourth terms 'b' and 'c' explain the magnitude and nature of magnetocrystalline anisotropy which are proportional to K^2 and K^3 respectively, where K is the magnetocrystalline anisotropy induced in the material. 'χ' represents the paramagnetic contribution existed towards magnetization. LAS fitted parameters of $CoFe_2O_4$ and $BaFe_2O_4$ are tabulated in table 3.4.

Table 3.4 Fitted parmaeters of $CoFe_2O_4$ and $BaFe_2O_4$ from LAS fitting

Compound	M_s (emu/g)	a (Oe)	b (x 10^6 Oe^2)	c (x 10^9 Oe^3)	χ (x $10^{-6}Oe^{-1}$)
$CoFe_2O_4$	85.44	594.28	3.06	-11.16	4.44
$BaFe_2O_4$	1.48	1271.40	16.14	-75.25	5.46

It is found that the inhomogeneity parameter is higher for $BaFe_2O_4$ and this larger value of inhomogeneity indicates either influence of structural defect or non-magnetic ions. From UV visible absorbance studies $BaFe_2O_4$ has low defect states compared to $CoFe_2O_4$ and it will discuss in detail. Therefore, here the larger value of the

inhomogeneity parameter of $BaFe_2O_4$ is mainly due to the presence of non-magnetic Ba ions. In terms of paramagnetic contribution, it is found that $BaFe_2O_4$ has a larger paramagnetic contribution than $CoFe_2O_4$ due to the non-magnetic nature of Ba ions. This confirms the coexistence of weak antiferromagnetism with ferrimagnetism in $BaFe_2O_4$. Comparing b and c values, it is seen that both $CoFe_2O_4$ and $BaFe_2O_4$ exhibit negative magnetocrystalline anisotropy. The high values of b and c parameters indicates that magnetocrystalline anisotropy is more in $BaFe_2O_4$. Besides the anisotropy contribution, the increase in coercivity of $BaFe_2O_4$ is due to the presence of non-magnetic Ba ions too. The non-magnetic behaviour of Ba ions produces inhomogeneity in magnetic domains, as a result, the system needs more energy to rotate magnetic moments from the easy axis to the hard axis.

3.4 Dielectric Studies

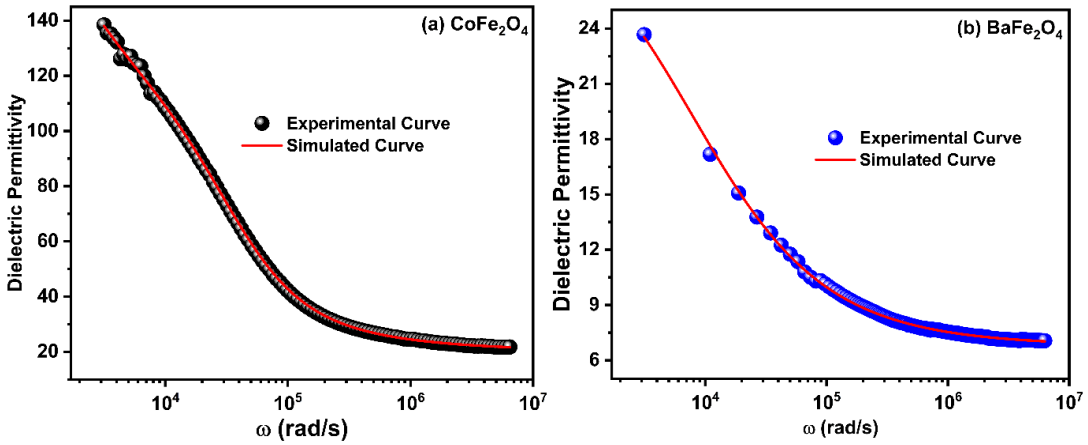

Figure 3.10 Frequency response curve of dielectric permittivity of (a) $CoFe_2O_4$ and (b) $BaFe_2O_4$

Figure 3.10 shows the variation of dielectric permittivity of $CoFe_2O_4$ and $BaFe_2O_4$ with respect to the frequency from 500 Hz to 1 MHz region. It is seen that in both samples, higher dielectric permittivity occurred in the lower frequency region and it exponentially decreases with increasing frequency and attains a constant value at higher frequencies. This frequency dispersion of dielectric permittivity is mainly explained by Maxwell Wagner polarization which is explained by Koop's phenomenon. According to this phenomenon, the high values of dielectric permittivity at the lower frequency region are due to the large capacitance value of poorly conducting grain boundaries than conducting grains. Due to this larger capacitance, the charge carriers are accumulated in grain boundaries which leads to the onset of interfacial or space charge

polarization. In the higher frequency region, the dipoles present in the material are unable to respond in the direction of a fast-changing electric field. As a result, a decrease in dielectric permittivity occurred in the high-frequency region.

From the figure, it is found that $CoFe_2O_4$ have larger dielectric permittivity than $BaFe_2O_4$. This high dielectric permittivity of $CoFe_2O_4$ is mainly due to the conductive nature of Co ions compared to Ba ions. From the literature, it is observed that the electrical resistivity of Ba ions (332 nΩ.m) is greater than Co ions (62.4 nΩ.m). This low electrical resistivity of Co ions increases the conductivity contribution in $CoFe_2O_4$ and it increases the dielectric permittivity. In order to reveal the dielectric relaxation mechanisms that occurred in the dielectric permittivity of $CoFe_2O_4$ and $BaFe_2O_4$ and to study the effect of conductivity, the dielectric dispersion curve is analysed with the help of the Havriliak Negami function associated with conductivity term and it is given below [65].

$$\boldsymbol{\varepsilon^* = \varepsilon_\infty + \frac{\varepsilon_0 - \varepsilon_\infty}{\left(1+(i\omega\tau)^{1-\alpha}\right)^{\beta}} + j\frac{\sigma^*}{\varepsilon_0 \omega^n}} \qquad \textbf{(17)}$$

Here, ε_s and ε_∞ represent the dielectric permittivities at low and higher frequency regions, respectively, and $\varepsilon_s - \varepsilon_\infty$ is the relaxation strength that occurred in the samples, and τ represents the mean relaxation time. α and β describe the asymmetricity and broadening of the dielectric dispersion curve and it resides between 0 and 1. If the α value becomes 0, then the equation becomes the Cole-Davidson model and if β becomes 1, then the equation becomes the Cole-Cole model. If both α and β become 0 and 1 respectively, then the equation satisfies the ideal debye model. '**σ**' represents the contribution of conductivity in dielectric relaxation and the n value gives the nature of conductivity. For n = 0, the dc conductivity is prominent and for $n \neq 0$ then the ac conductivity becomes prominent. The parameters obtained from the fitting of the dielectric dispersion curve of $CoFe_2O_4$ and $BaFe_2O_4$ are summarized in table 3.5.

Table 3.5 Parameters obtained from the fitting of the dielectric dispersion curve of $CoFe_2O_4$ and $BaFe_2O_4$

Compound	ε_∞	ε_s	τ x 10^{-5} (sec)	α	β	σ x 10^{-8}(S/m)	n
$CoFe_2O_4$	20.06	50.85	3.01	0.14	1	1.90	0.47
$BaFe_2O_4$	6.80	18.12	12.70	0.39	1	0	0

From the table, it is observed that the β value is equal to 1 which indicates that dielectric relaxation of $CoFe_2O_4$ and $BaFe_2O_4$ occurred by the cole-cole relaxation model. It means that the dielectric relaxation in $CoFe_2O_4$ and $BaFe_2O_4$ is contributed by multiple ions instead of Fe ions only. It is also found that the α value is smaller for $CoFe_2O_4$ which indicates the spreading of relaxation times in $CoFe_2O_4$ is smaller than $BaFe_2O_4$. The spreading relaxation time largely depends upon the free charge concentration and localized defect states in the material. From UV-Visible studies, it is confirmed that the free charge carrier concentration is smaller for $CoFe_2O_4$ when compared to $BaFe_2O_4$ and this is due to the trapping of charge carriers in defective states of the system, which will discuss in detail. This trapping of charge carriers reduces the contribution of multiple ions in relaxation which reduces the spreading of relaxation times in $CoFe_2O_4$. From the table, it is revealed that the dielectric permittivity of $CoFe_2O_4$ largely depends on the conductive nature of metal ions present in the system and it exhibits a small conductivity value of 1.98 x 10^{-8} (S/m). However, due to the larger electric resistivity of Ba ions, the conductivity contribution is zero in the case of $BaFe_2O_4$.

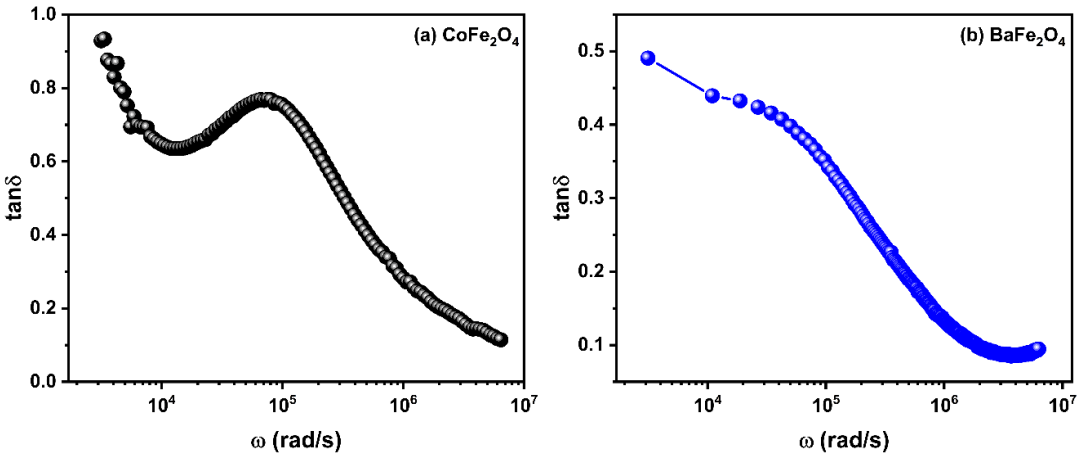

Figure 3.11 Dielectric loss factor with respect to frequency of (a) $CoFe_2O_4$ and (b) $BaFe_2O_4$

Figure 3.11 shows the variation of tangent loss of $CoFe_2O_4$ and BaFe2O4 with respect to frequency. It is seen that tangent loss decreases with increasing frequency. At low frequency, the resistivity of samples becomes very large, therefore to exchange electrons in between cations high energy is needed, which in turn contributes to the high dielectric loss. With increasing frequency, the energy needed for electron exchange reduces, and it leads to a decrease in the dielectric loss factor. From the figure, it is found that $BaFe_2O_4$ has a low tangent loss compared to $CoFe_2O_4$ and it is

due to the large electrical resistivity of Ba ions. The large electrical resistivity reduces energy loss occurred by eddy current which is very useful to use in transformer applications. In $CoFe_2O_4$ a resonance peak is observed and it indicates that the hopping frequency of localized charge carriers becomes equal to the frequency of the applied electric field. However, in $BaFe_2O_4$, this resonance peak is absent due to the absence of localized charge carriers. The presence of localized charge carriers depends on the density of localized energy states that occurred in between the conduction band and valence band. From UV-Visible absorption studies, it is found that $CoFe_2O_4$ exhibit a large number of localized states than $BaFe_2O_4$.

3.5 Optical Studies

UV-Visible spectroscopy is a versatile analytical technique to study the optical properties of samples in the ultraviolet-visible region. The reflectance spectrum of pure $CoFe_2O_4$ and $BaFe_2O_4$ in the wavelength range of 200-800 nm is shown in figure 3.12. From the figure, it is seen that the reflectance of $BaFe_2O_4$ increases and $CoFe_2O_4$ decreases with the wavelength in the UV region. It remains constant throughout the visible region of the spectrum. On further increasing wavelength into the near IR region there is a rapid increase in reflectance. It is found that $BaFe_2O_4$ shows a higher diffuse reflectance than $CoFe_2O_4$. It is mainly due to the larger defect states that occurred in the $CoFe_2O_4$ system that trap the free charge carriers in these localized defect states and it is confirmed by band gap and Urbach energy studies.

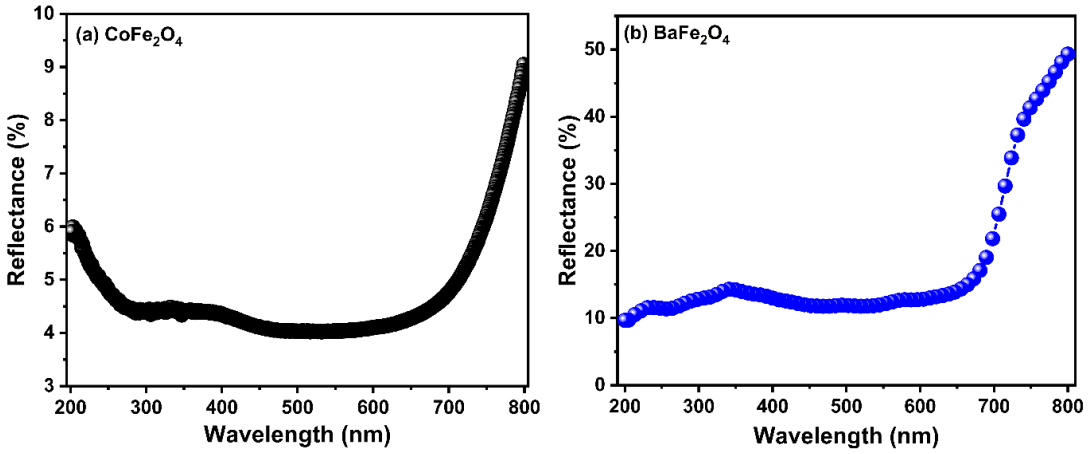

Figure 3.12 Reflectance spectrum of (a) $CoFe_2O_4$ and (b) $BaFe_2O_4$

To determine the optical band gap of $CoFe_2O_4$ and $BaFe_2O_4$, the Tauc plot relation is used which is given by,

$$\alpha h\nu = A\,(h\nu - E_g)^n \qquad (18)$$

where α is the absorption coefficient, hν is the incident photon energy, A is the energy independent constant, E_g is the optical band gap of the material and n denotes the nature of the electronic transition. To find the band gap, a graph is plotted between $(\alpha h\nu)^{1/n}$ and hν for different values of n. If the plot shows a linear part for n=1/2, then the material exhibit a direct allowed transition and for n=2 they exhibit an indirect allowed transition. According to Tauc's relation, the band gap of the material can be obtained by extrapolating the linear part to zero absorption coefficient. To study the optical properties of the solid sample we use diffuse reflectance spectroscopy. The optical absorption coefficient can be calculated from the reflectance data by using the Kubelka-Munk function given by [66–68],

$$F(R_\infty) = \frac{(1-R_\infty)^2}{2R_\infty} \qquad (19)$$

where R_∞ is the reflectance of the material at infinite thickness. Applying the Kubelka-Munk function in the tauc's relation we get,

$$F(R_\infty)\, h\nu = A(h\nu - E_g)^n \qquad (20)$$

It is observed that for $CoFe_2O_4$ and $BaFe_2O_4$ tauc relation is followed at n = 1/2. It means that in both these compounds occurred a direct allowed electronic transition in UV visible region. The plot of $[F(R_\infty)h\nu]^2$ versus hν of $CoFe_2O_4$ and $BaFe_2O_4$ is shown in figure 3.13. It is found that both $CoFe_2O_4$ and $BaFe_2O_4$ shows two slope variation in the UV-visible region and it is denoted as E_{g1} and E_{g2} in figure 3.13. E_{g2} represents the optical band gap of the material and E_{g1} represents the defect gap that occurred in the material by localized states between the conduction band and valence band. It is observed that $BaFe_2O_4$ exhibit a larger band gap than $CoFe_2O_4$. The defect band gap which means the gap between the valence band or conduction band to defect states is also greater for $BaFe_2O_4$. However, the difference between the optical band gap and the defect gap is greater for $BaFe_2O_4$ due to the low density of localized states in between the conduction and valence bands.

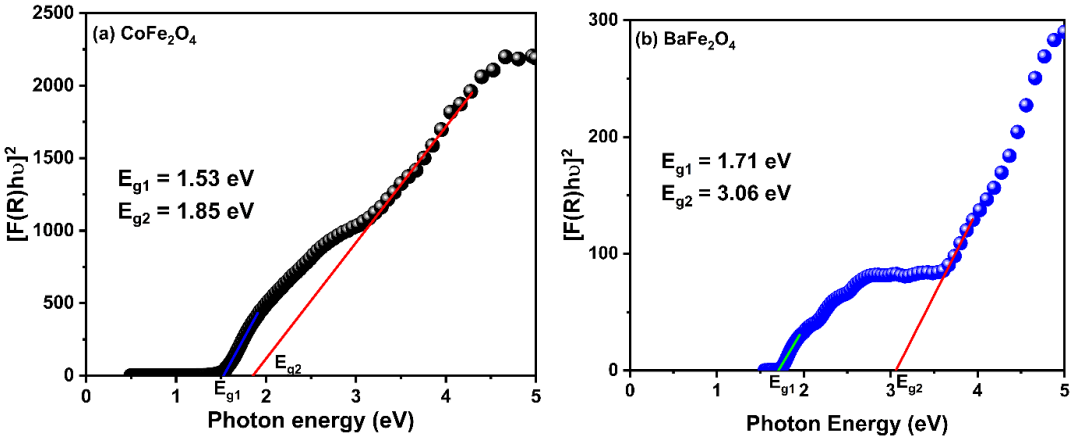

Figure 3.13 Estimation of direct and defect band gap of (a) $CoFe_2O_4$ and (b) $BaFe_2O_4$

The defect states create a band tail extending from the lower conduction band to the band gap. Similarly, the defect states very near to the valence band also smears the valence band edge deep inside the gap. Thus a shallow defect band is formed in between the conduction band and valence band. These defects trap the excited electrons and prevent the direct transition of electrons between the valence band and conduction band. Hence it forms a forbidden energy gap in the optical band gap. The energy associated with this forbidden gap is the Urbach energy. Urbach energy is obtained from the relation [68],

$$\alpha = \alpha_0 \exp\left[\frac{h\nu}{E_u}\right] \qquad (21)$$

where E_u is the Urbach energy. Figure 3.14 shows the variation of ln F(R) versus photon energy hν for $CoFe_2O_4$ and $BaFe_2O_4$. The reciprocal of the slope of these graphs give the Urbach energy of the samples. From the figure, it is found that the Urbach energy is higher for $CoFe_2O_4$ indicating the presence of a larger amount of localized states. The low density of localized states in $BaFe_2O_4$ indicates it almost has a defect-free crystal system which reduces the energy loss occurred by the eddy currents

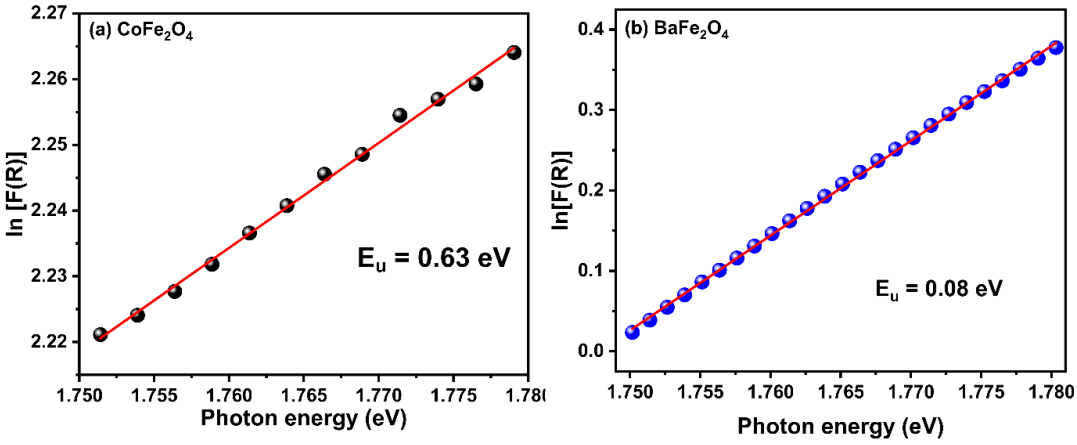

Figure 3.14 Urbach's Plot (a) $CoFe_2O_4$ and (b) $BaFe_2O_4$

It is well known that the polarizability of any solid is proportional to its complex dielectric constant. The complex dielectric function has two components and is expressed as [68],

$$\varepsilon^* = \varepsilon_{real} + i\varepsilon_{imaginary} \qquad (22)$$

Where ε_{real} represents the real dielectric permittivity of material which gives the dispersion rate of an incident photon in the sample, in other words it helps to study the slowdown of an incident photon in the material during absorption. $\varepsilon_{imaginary}$ represents the imaginary dielectric permittivity which explains how the sample absorbs energy from the electric field due to dipole motion throughout the UV-visible region. ε^* is an important quantity for designing highly efficient optoelectronic and magneto-optic devices. The values of real and imaginary parts of the dielectric constant are given by,

$$\varepsilon_{real} = n^2 - k^2 \qquad (23)$$

$$\varepsilon_{imaginary} = 2nk \qquad (24)$$

Figure 3.15 shows the variation of the real dielectric permittivity of $CoFe_2O_4$ and $BaFe_2O_4$ as a function of incident photon energy. It is found that the real dielectric permittivity decreases with increasing photon energy in both cases. It is mainly due to the trapping of charge carriers in defect states in higher photon energy, as a result, the hopping rate of Fe^{2+}-Fe^{3+} ions is restricted with increasing photon energy. The larger real dielectric permittivity of $BaFe_2O_4$ is mainly due to the lowest defect states in the system which reduces trapping of free charge carriers which increases the hopping Fe^{2+}-Fe^{3+} ions and it results in higher dielectric permittivity than $CoFe_2O_4$.

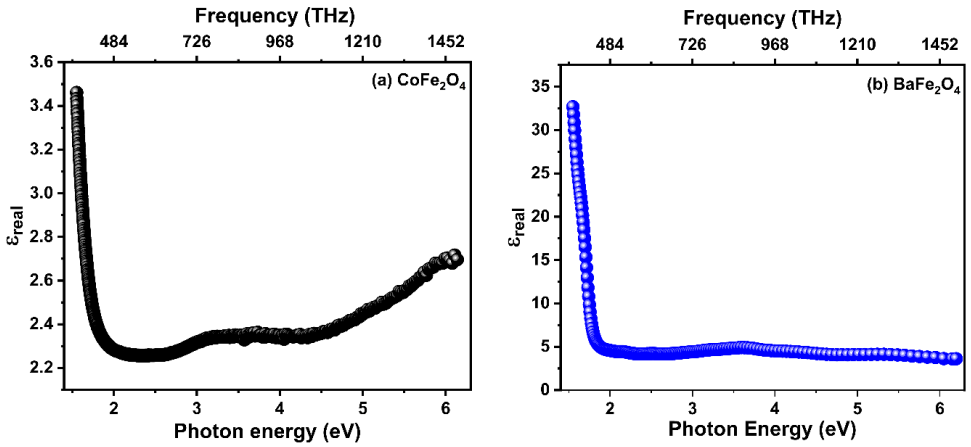

Figure 3.15 Variation of ε_{real} with photon energy (a) $CoFe_2O_4$ and (b) $BaFe_2O_4$

The variation of imaginary dielectric permittivity as a function of the incident photon energy of $CoFe_2O_4$ and $BaFe_2O_4$ is shown in figure 3.16. From the figure, it is seen that the imaginary dielectric permittivity first increases with photon energy and attains a maximum value at photon energy around 1.85 eV and 1.95 eV for $CoFe_2O_4$ and $BaFe_2O_4$ respectively. On further increasing of photon energy reduces the imaginary dielectric permittivity of both materials. The increase of imaginary dielectric permittivity is mainly due to the restriction of hopping between Fe^{2+}- Fe^{3+} ions by the trapping of free charge carriers in defect states. In higher photon energy, free charge carriers have enough energy to hop between Fe^{2+}- Fe^{3+} ions, as a result, imaginary dielectric permittivity decreases with increasing photon energy. It means that the dissipative rate or energy loss during the electron interaction and electromagnetic radiation decreases with increasing energy at higher photon energy. The low density localized defect states in $BaFe_2O_4$ tends smaller energy loss than $CoFe_2O_4$.

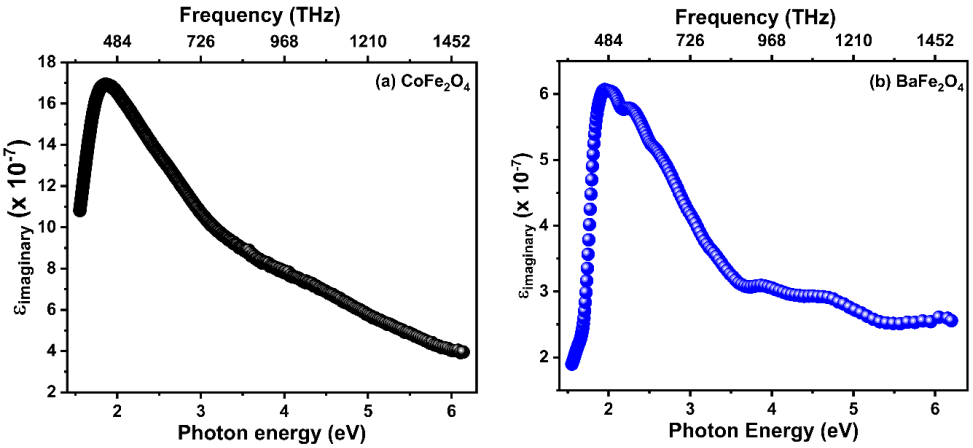

Figure 3.16 Variation of $\varepsilon_{imaginary}$ with photon energy (a) $CoFe_2O_4$ and (b) $BaFe_2O_4$

This dispersion of dielectric properties arises from the motion of free charge carriers and bound carriers. To study the influence of free charge carriers, the lattice dielectric constant (ε_L) and the free carrier concentration within the effective mass (N/m*) are calculated. The expression used for calculating ε_L and N/m* related to the refractive index is given as [68],

$$n^2 = \varepsilon_L - \left(\frac{e^2}{4\pi c^2 \varepsilon_0}\right)\left(\frac{N}{m^*}\right)\lambda^2 \qquad (25)$$

Here, e is the elementary charge ε_0 is the absolute permittivity in free space. The ε_L and N/m* are obtained from the intercept and slope of the n^2 versus λ^2 plot. The plot between n^2 and λ^2 of $CoFe_2O_4$ and $BaFe_2O_4$ is shown in figure 3.17. It is observed that $BaFe_2O_4$ shows a high lattice dielectric constant than $CoFe_2O_4$ due to the orthorhombic structure with non-centrosymmetricity. The non-centrosymmetric structure is most favourable for inducing spontaneous polarization by atomic polarizability. Besides structural properties, a large number of free charge carriers in $BaFe_2O_4$ also increases the hopping rate between cations which enhances polarization in the system. The low concentration defect states reduce the trapping of free charge carriers, therefore, $BaFe_2O_4$ shows a large amount of free charge carrier concentration.

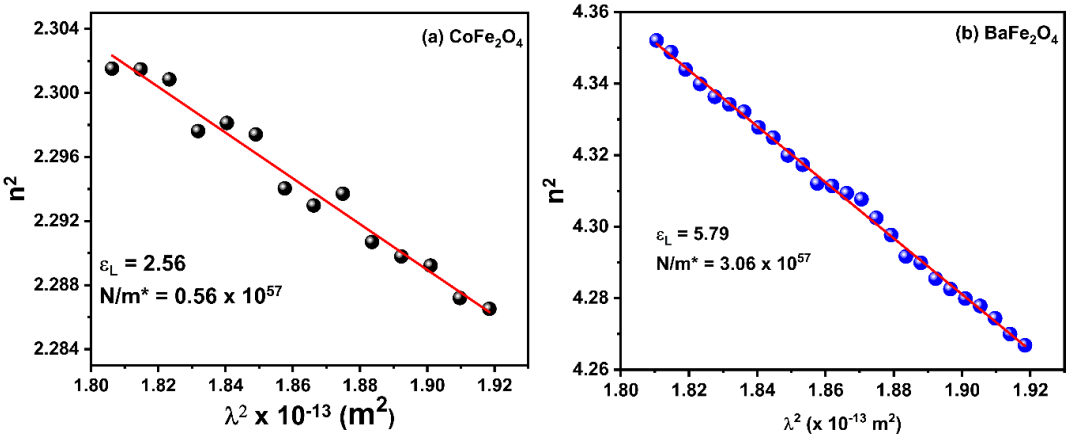

Figure 3.17 Plot between n^2 and λ^2 of (a) $CoFe_2O_4$ and (b) $BaFe_2O_4$

The bound carriers effect in the material can be studied with the help of the Moss model. According to the Moss model, the effect of free charge carrier concentration is negligible in the high-frequency region. The motion of bound carriers produces a high-frequency dielectric constant in the material and it is related to the refractive index. The relation between static dielectric constant and refractive index is given as [68],

$$\frac{n_s^2 - 1}{n^2 - 1} = 1 - \left(\frac{\lambda_0}{\lambda}\right)^2 \qquad (26)$$

Here, n_s represents the static refractive index of the material and λ_0 is the inter-band oscillator wavelength. Static refractive index and inter-band oscillator wavelength are determined from the slope and intercept of $(n^2\text{-}1)^{-1}$ versus λ^{-2} plot. The high-frequency dielectric constant is a square of the static refractive index ($\varepsilon_\infty = n_s^2$). The graph between $(n^2\text{-}1)^{-1}$ versus λ^{-2} for $CoFe_2O_4$ and $BaFe_2O_4$ is shown in figure 3.18.

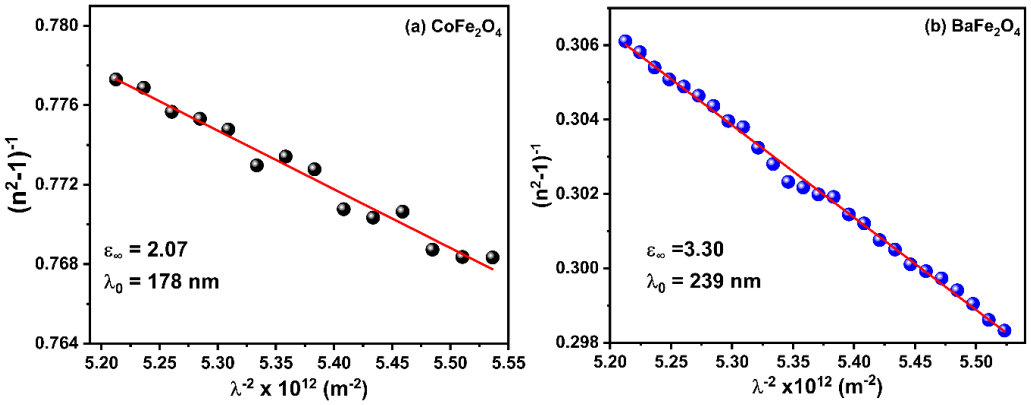

Figure 3.18 Plot of $(n^2\text{-}1)^{-1}$ versus λ^2 of (a) $CoFe_2O_4$ and (b) $BaFe_2O_4$

From the figure, it is found that the free charge carrier contribution is more dominant compared to the bound carriers contribution. Comparing the electronic structure of Co ions and Ba ions, Ba ions have a large number of electrons present in the inner shell which increases the number of bound electrons in the material. This large number of bound electrons gives a higher value of dielectric constant due to bound carriers in $BaFe_2O_4$ than $CoFe_2O_4$.

Chapter 4
Conclusions

Cobalt ferrite and barium ferrite are two well-known ferrite systems with transition metal and alkaline earth metal in the divalent metal ion position respectively. Single phasic $CoFe_2O_4$ and $BaFe_2O_4$ samples were successfully prepared via the sol-gel method. Rietveld refined XRD patterns of $CoFe_2O_4$ and $BaFe_2O_4$ revealed that $CoFe_2O_4$ exhibits a centrosymmetric mixed spinel cubic structure with space group *Fd-3m* and BaFe2O4 exhibits a non-centrosymmetric orthorhombic structure with a space group $Cmc2_1$. This non-centrosymmetric crystal structure of $BaFe_2O_4$ is highly favourable to induce spontaneous polarization which could tends to exhibit ferroelectric.

Magnetic studies reveal that $CoFe_2O_4$ exhibit higher magnetic properties than $BaFe_2O_4$. $CoFe_2O_4$ exhibits a ferrimagnetic behaviour and $BaFe_2O_4$ exhibit ferrimagnetism with weak antiferromagnetism. These anomalous magnetic properties of $BaFe_2O_4$ are mainly due to the high magnetocrystalline anisotropy and the presence of non-magnetic Ba ions.

Dielectric properties show that both $CoFe_2O_4$ and $BaFe_2O_4$ exhibit cole-cole model dielectric relaxation mechanisms. $CoFe_2O_4$ has a larger dielectric permittivity than $BaFe_2O_4$ and it is due to the additional conductivity contribution that occurred in $CoFe_2O_4$. However, in terms of dielectric loss factor, $BaFe_2O_4$ is a good material which has a low loss factor. This low loss factor is mainly due to the almost defect-free crystal system of $BaFe_2O_4$ and it is confirmed by optical studies.

Optical studies reveal that the reflectance of $CoFe_2O_4$ is smaller than $BaFe_2O_4$ and it is due to the high density of localized states of $CoFe_2O_4$ in between the conduction band and valence band. This variation of localized states is confirmed by evaluating Urbach energy. The larger localized states of $CoFe_2O_4$ trap the charge carrier and it reduces the free charge carrier concentration in the system. The defect-free crystal system of $BaFe_2O_4$ gives a large number of free charge carrier concentrations which reduces the energy loss occurred in the material. It is found that $BaFe_2O_4$ shows high lattice dielectric constant than $CoFe_2O_4$ due to the non-centrosymmetric structure of the crystal.

Chapter 5
Future scope of the work

Magnetism and ferroelectricity, the significance of these two fields never fade due to their wide range of applications in science and technology. Combining these two phenomena into a single phase opens a new window for the scientific world to develop a new era of sensors and memory devices. In this work, we found a defect-free material $BaFe_2O_4$ has good dielectric properties and it can achieve ferroelectricity at room temperature. However, the magnetic properties of $BaFe_2O_4$ are not so good that compared to other MFe_2O_4 materials. Therefore, rare earth (RE) substitution in Ba or Fe sites can help to improve the magnetic properties of $BaFe_2O_4$. Besides RE substitution, a proper combination of Co and Ba ions in M sites of MFe_2O_4 will give good multiferroic material system in future.

References

[1] M.A. Wahab, Solid State Physics, Narosa Publishing House , 1999.

[2] R. Puri, V. Babbar, Solid State Physics and Electronics, S. Chand Limited, 2008.

[3] Interfacial Polarization, (n.d.). https://www.sciencedirect.com/topics/engineering/interfacial-polarization#:~:text=The%20space%20charge%2C%20or%20interfacial,the%20interfaces%20between%20different%20materials. (accessed August 29, 2022).

[4] Capacitor Fundamentals: Part 4 – Dielectric Polarization, (n.d.). https://blog.knowlescapacitors.com/blog/capacitor-fundamentals-part-4-dielectric-polarization (accessed August 30, 2022).

[5] R.N. Fadhil, The Effect of Aluminum and Copper Powder on the Physical properties of the Epoxy Composite, 2018.

[6] C. Kittel, Introduction to Solid State Physics, John Wiley & sons ltd. , 2010.

[7] J.S. Galsin, Solid State Physics: An introduction to theory, Academics press , 2019.

[8] J. Coey, Magnetism and Magnetic Materials , Cambridge University Press, 2009.

[9] K.J. Standley, Oxide magnetic materials , Oxford, Clarendon Press, 1962.

[10] V. v. Jadhav, S.D. Shirsat, U.B. Tumberphale, R.S. Mane, Properties of ferrites, in: Spinel Ferrite Nanostructures for Energy Storage Devices, Elsevier, 2020: pp. 35–50. https://doi.org/10.1016/B978-0-12-819237-5.00003-1.

[11] S.K. Gore, S.S. Jadhav, Basics of ferrites, in: Spinel Ferrite Nanostructures for Energy Storage Devices, Elsevier, 2020: pp. 1–11. https://doi.org/10.1016/B978-0-12-819237-5.00001-8.

[12] M. Usman, Studies of Ferroelectric and Multiferroic Behavior in [Ba(Zr,Ti)O3]1-y:[CoFe2O4]y System, 2015.

[13] H.-W. Zhang, J. Li, H. Su, T.-C. Zhou, Y. Long, Z.-L. Zheng, Development and application of ferrite materials for low temperature co-fired ceramic technology,

Chinese Physics B. 22 (2013) 117504. https://doi.org/10.1088/1674-1056/22/11/117504.

[14] A. Moitra, S. Kim, S.-G. Kim, S.C. Erwin, Y.-K. Hong, J. Park, Defect formation energy and magnetic properties of aluminum-substituted M-type barium hexaferrite, Computational Condensed Matter. 1 (2014) 45–50. https://doi.org/10.1016/j.cocom.2014.11.001.

[15] W.W. Supplee, Structural, magnetic, and optical properties of orthoferrite thin films, (n.d.). http://hdl.handle.net/1721.1/44813 (accessed August 30, 2022).

[16] T. Tatarchuk, M. Bououdina, J. Judith Vijaya, L. John Kennedy, Spinel Ferrite Nanoparticles: Synthesis, Crystal Structure, Properties, and Perspective Applications, in: 2017: pp. 305–325. https://doi.org/10.1007/978-3-319-56422-7_22.

[17] Y. Qu, H. Yang, N. Yang, Y. Fan, H. Zhu, G. Zou, The effect of reaction temperature on the particle size, structure and magnetic properties of coprecipitated CoFe2O4 nanoparticles, Mater Lett. 60 (2006) 3548–3552. https://doi.org/10.1016/j.matlet.2006.03.055.

[18] L. Yang, G. Xi, T. Lou, X. Wang, J. Wang, Y. He, Preparation and magnetic performance of Co 0.8 Fe 2.2 O 4 by a sol–gel method using cathode materials of spent Li-ion batteries, Ceram Int. 42 (2016) 1897–1902. https://doi.org/10.1016/j.ceramint.2015.09.159.

[19] R. Safi, A. Ghasemi, R. Shoja-Razavi, M. Tavousi, The role of pH on the particle size and magnetic consequence of cobalt ferrite, J Magn Magn Mater. 396 (2015) 288–294. https://doi.org/10.1016/j.jmmm.2015.08.022.

[20] E. Swatsitang, S. Phokha, S. Hunpratub, B. Usher, A. Bootchanont, S. Maensiri, P. Chindaprasirt, Characterization and magnetic properties of cobalt ferrite nanoparticles, J Alloys Compd. 664 (2016) 792–797. https://doi.org/10.1016/j.jallcom.2015.12.230.

[21] M. Cernea, P. Galizia, I. Ciuchi, G. Aldica, V. Mihalache, L. Diamandescu, C. Galassi, CoFe 2 O 4 magnetic ceramic derived from gel and densified by spark

plasma sintering, J Alloys Compd. 656 (2016) 854–862. https://doi.org/10.1016/j.jallcom.2015.09.271.

[22] X. Yang, X. Wang, Z. Zhang, Electrochemical properties of submicron cobalt ferrite spinel through a co-precipitation method, J Cryst Growth. 277 (2005) 467–470. https://doi.org/10.1016/j.jcrysgro.2005.02.004.

[23] B. Peeples, V. Goornavar, C. Peeples, D. Spence, V. Parker, C. Bell, D. Biswal, G.T. Ramesh, A.K. Pradhan, Structural, stability, magnetic, and toxicity studies of nanocrystalline iron oxide and cobalt ferrites for biomedical applications, Journal of Nanoparticle Research. 16 (2014) 2290. https://doi.org/10.1007/s11051-014-2290-9.

[24] D.-H. Kim, D.E. Nikles, D.T. Johnson, C.S. Brazel, Heat generation of aqueously dispersed CoFe2O4 nanoparticles as heating agents for magnetically activated drug delivery and hyperthermia, J Magn Magn Mater. 320 (2008) 2390–2396. https://doi.org/10.1016/j.jmmm.2008.05.023.

[25] P. Kumar, S.K. Sharma, M. Knobel, M. Singh, Effect of La3+ doping on the electric, dielectric and magnetic properties of cobalt ferrite processed by co-precipitation technique, J Alloys Compd. 508 (2010) 115–118. https://doi.org/10.1016/j.jallcom.2010.08.007.

[26] Y.D. Kolekar, L. Sanchez, E.J. Rubio, C.V. Ramana, Grain and grain boundary effects on the frequency and temperature dependent dielectric properties of cobalt ferrite–hafnium composites, Solid State Commun. 184 (2014) 34–39. https://doi.org/10.1016/j.ssc.2013.12.003.

[27] O.M. Lemine, M. Bououdina, M. Sajieddine, A.M. Al-Saie, M. Shafi, A. Khatab, M. Al-hilali, M. Henini, Synthesis, structural, magnetic and optical properties of nanocrystalline ZnFe2O4, Physica B Condens Matter. 406 (2011) 1989–1994. https://doi.org/10.1016/j.physb.2011.02.072.

[28] S. Mandizadeh, M. Salavati-Niasari, M. Sadri, Hydrothermal synthesis, characterization and magnetic properties of BaFe2O4 nanostructure as a photocatalytic oxidative desulfurization of dibenzothiophene, Sep Purif Technol. 175 (2017) 399–405. https://doi.org/10.1016/j.seppur.2016.11.071.

[29] W.S. Galvão, D.M.A. Neto, R.M. Freire, P.B.A. Fechine, Super-Paramagnetic Nanoparticles with Spinel Structure: A Review of Synthesis and Biomedical Applications, Solid State Phenomena. 241 (2015) 139–176. https://doi.org/10.4028/www.scientific.net/SSP.241.139.

[30] H. Mitsuda, S. Mori, C. Okazaki, The crystal structure of barium monoferrite, BaFe2O4, Acta Crystallogr B. 27 (1971) 1263–1269. https://doi.org/10.1107/S0567740871003832.

[31] K. Maaz, A. Mumtaz, S.K. Hasanain, A. Ceylan, Synthesis and magnetic properties of cobalt ferrite (CoFe2O4) nanoparticles prepared by wet chemical route, J Magn Magn Mater. 308 (2007) 289–295. https://doi.org/10.1016/j.jmmm.2006.06.003.

[32] Z. Zi, Y. Sun, X. Zhu, Z. Yang, J. Dai, W. Song, Synthesis and magnetic properties of CoFe2O4 ferrite nanoparticles, J Magn Magn Mater. 321 (2009) 1251–1255. https://doi.org/10.1016/j.jmmm.2008.11.004.

[33] D. Zhao, X. Wu, H. Guan, E. Han, Study on supercritical hydrothermal synthesis of CoFe2O4 nanoparticles, J Supercrit Fluids. 42 (2007) 226–233. https://doi.org/10.1016/j.supflu.2007.03.004.

[34] R. Zhang, L. Sun, Z. Wang, W. Hao, E. Cao, Y. Zhang, Dielectric and magnetic properties of CoFe2O4 prepared by sol-gel auto-combustion method, Mater Res Bull. 98 (2018) 133–138. https://doi.org/10.1016/j.materresbull.2017.08.006.

[35] C.-H. Yan, Z.-G. Xu, F.-X. Cheng, Z.-M. Wang, L.-D. Sun, C.-S. Liao, J.-T. Jia, Nanophased CoFe 2 O 4 prepared by combustion method, Solid State Commun. 111 (1999) 287–291. https://doi.org/10.1016/S0038-1098(99)00119-2.

[36] V. Kumar, A. Rana, M.S. Yadav, R.P. Pant, Size-induced effect on nano-crystalline CoFe2O4, J Magn Magn Mater. 320 (2008) 1729–1734. https://doi.org/10.1016/j.jmmm.2008.01.021.

[37] M.C. Dimri, H. Khanduri, P. Agarwal, J. Pahapill, R. Stern, Structural, magnetic, microwave permittivity and permeability studies of barium monoferrite (BaFe2O4), J Magn Magn Mater. 486 (2019) 165278. https://doi.org/10.1016/j.jmmm.2019.165278.

[38] S. da Dalt, B.B. Sousa, A.K. Alves, C.P. Bergmann, Structural and photocatalytic characterization of BaFe2O4 obtained at low temperatures, Materials Research. 14 (2011) 505–507. https://doi.org/10.1590/S1516-14392011005000069.

[39] S. Mandizadeh, M. Salavati-Niasari, M. Sadri, Hydrothermal synthesis, characterization and magnetic properties of BaFe2O4 nanostructure as a photocatalytic oxidative desulfurization of dibenzothiophene, Sep Purif Technol. 175 (2017) 399–405. https://doi.org/10.1016/j.seppur.2016.11.071.

[40] A. JAAFAR, S. AREKAT, A. AL-SAIE, M. BOUOUDINA, STRUCTURE AND MAGNETIC PROPERTIES OF NANOSIZED BaFe 2 O 4 MATERIAL, Int J Nanosci. 09 (2010) 575–577. https://doi.org/10.1142/S0219581X10007289.

[41] R. Peymanfar, M. Rahmanisaghieh, A. Ghaffari, Y. Yassi, Preparation and Identification of BaFe2O4 Nanoparticles by the Sol–Gel Route and Investigation of Its Microwave Absorption Characteristics at Ku-Band Frequency Using Silicone Rubber Medium, in: The 3rd International Electronic Conference on Materials Sciences, MDPI, Basel Switzerland, 2018: p. 5234. https://doi.org/10.3390/ecms2018-05234.

[42] A. Javidan, M. Ramezani, A. Sobhani-Nasab, S.M. Hosseinpour-Mashkani, Synthesis, characterization, and magnetic property of monoferrite BaFe2O4 nanoparticles with aid of a novel precursor, Journal of Materials Science: Materials in Electronics. 26 (2015) 3813–3818. https://doi.org/10.1007/s10854-015-2907-5.

[43] K.M. Batoo, D. Salah, G. Kumar, A. Kumar, M. Singh, M. Abd El-Sadek, F.A. Mir, A. Imran, D.A. Jameel, Hyperfine interaction and tuning of magnetic anisotropy of Cu doped CoFe2O4 ferrite nanoparticles, J Magn Magn Mater. 411 (2016) 91–97. https://doi.org/10.1016/j.jmmm.2016.03.058.

[44] P. Anjana, R.S.A. Raj, R. Jose, M. Kumari, P.M. Sarun, D. Sajan, L.K. Joy, Highly enhanced dielectric permittivity in CoFe2O4 by the Gd substitution in the octahedral sites, J Alloys Compd. 854 (2021) 155758. https://doi.org/10.1016/j.jallcom.2020.155758.

[45] Y.X. Zheng, Q.Q. Cao, C.L. Zhang, H.C. Xuan, L.Y. Wang, D.H. Wang, Y.W. Du, Study of uniaxial magnetism and enhanced magnetostriction in magnetic-annealed polycrystalline CoFe2O4, J Appl Phys. 110 (2011) 043908. https://doi.org/10.1063/1.3624661.

[46] S. Ayyappan, J. Philip, B. Raj, A facile method to control the size and magnetic properties of CoFe2O4 nanoparticles, Mater Chem Phys. 115 (2009) 712–717. https://doi.org/10.1016/j.matchemphys.2009.02.005.

[47] S.E. Shirsath, D. Wang, S.S. Jadhav, M.L. Mane, S. Li, Ferrites Obtained by Sol-Gel Method, in: Handbook of Sol-Gel Science and Technology, Springer International Publishing, Cham, 2018: pp. 695–735. https://doi.org/10.1007/978-3-319-32101-1_125.

[48] A.V. Bagade, P.A. Nagwade, A.V. Nagawade, S.R. Thopate, S.N. Pund, A Review on Synthesis, Characterization and Applications of Cadmium Ferrite and its Doped Variants, Oriental Journal Of Chemistry. 38 (2022) 01–15. https://doi.org/10.13005/ojc/380101.

[49] B.D. CULLITY, Elements of X-RAY DIFFRACTION, Addison Wesley, 1978.

[50] S. Baskaran, Structure and regulation of yeast glycogen synthase, 2010.

[51] COMPONENT PARTS OF AN X-RAY DIFFRACTOMETER, (n.d.). https://xrd.co/category/x-ray-diffractometer/ (accessed August 30, 2022).

[52] J.S.O. Evans, I.R. Evans, Structure Analysis from Powder Diffraction Data: Rietveld Refinement in Excel, J Chem Educ. 98 (2021) 495–505. https://doi.org/10.1021/acs.jchemed.0c01016.

[53] R.W. Frei, Diffuse Reflectance Spectroscopy in Environmental, CRC Press , 1973.

[54] Schematic of UV- visible spectrophotometer, (n.d.). https://commons.wikimedia.org/wiki/File:Schematic_of_UV-_visible_spectrophotometer.png (accessed August 30, 2022).

[55] Z. Hanani, Design of flexible lead-free ceramic/biopolymer composite for energy storage and energy harvesting applications, 2020.

[56] E. Barsoukov, Impedance Spectroscopy, Wiley, 2005. https://doi.org/10.1002/0471716243.

[57] K.H.J. Buschow, Physics of Magnetism and Magnetic Materials , Springer, 2003.

[58] D. Jiles, Introduction to Magnetism and Magnetic Materials , CRC Press, 2015.

[59] B.D. Cullity, Introduction to magnetic materials , Wiley-IEEE Press, 2008.

[60] Advanced Magnetometry, (n.d.). https://magnetism.eu/esm/2005-constanta/slides/sander-slides.pdf (accessed August 30, 2022).

[61] V. Mote, Y. Purushotham, B. Dole, Williamson-Hall analysis in estimation of lattice strain in nanometer-sized ZnO particles, Journal of Theoretical and Applied Physics. 6 (2012) 6. https://doi.org/10.1186/2251-7235-6-6.

[62] R. Grössinger, A critical examination of the law of approach to saturation. I. Fit procedure, Physica Status Solidi (a). 66 (1981) 665–674. https://doi.org/10.1002/pssa.2210660231.

[63] J. Lee, E.J. Lee, T.-Y. Hwang, J. Kim, Y.-H. Choa, Anisotropic characteristics and improved magnetic performance of Ca–La–Co-substituted strontium hexaferrite nanomagnets, Sci Rep. 10 (2020) 15929. https://doi.org/10.1038/s41598-020-72608-0.

[64] S. Khalid, S. Riaz, S. Naeem, A. Akbar, S. Sajjad Hussain, Y. Xu, S. Naseem, Spin polarization and magneto-dielectric coupling in Al-modified thin iron oxide films -microwave mediated sol-gel approach, Journal of Industrial and Engineering Chemistry. 103 (2021) 49–66. https://doi.org/10.1016/j.jiec.2021.06.028.

[65] S. Havriliak, S.J. Havriliak, Comparison of the Havriliak-Negami and stretched exponential functions, Polymer (Guildf). 37 (1996) 4107–4110. https://doi.org/10.1016/0032-3861(96)00274-1.

[66] A. Somvanshi, S. Husain, W. Khan, Investigation of structure and physical properties of cobalt doped nano-crystalline neodymium orthoferrite, J Alloys Compd. 778 (2019) 439–451. https://doi.org/10.1016/j.jallcom.2018.11.095.

[67] A. Anantharaman, T.L. Ajeesha, JeenaN. Baby, M. George, Effect of structural, electrical and magneto-optical properties of CeMnxFe1-xO3-δ perovskite materials, Solid State Sci. 99 (2020) 105846. https://doi.org/10.1016/j.solidstatesciences.2019.02.007.

[68] K. Dincer, B. Waisi, G. Önal, N. Tuğluoğlu, J. McCutcheon, Ö.F. Yüksel, Investigation of optical and dispersion parameters of electrospinning grown activated carbon nanofiber (ACNF) layer, Synth Met. 237 (2018) 16–22. https://doi.org/10.1016/j.synthmet.2018.01.008.